https://ntrs.nasa.gov/search.jsp?R=19810022421 2020-03-21T12:48:39+00:00Z

NASA CONTRACTOR REPORT 165757

Optical Processing for Landmark Identification

DAVID CASASENT AND
THANH KY LUU

Carnegie-Mellon University
Department of Electrical Engineering
Pittsburgh, Pennsylvania 15213

CONTRACT NAS1-16125
SEPTEMBER 1981

National Aeronautics and
Space Administration

Langley Research Center
Hampton, Virginia 23665

TABLE OF CONTENTS

LIST OF FIGURES

LIST OF TABLES

ABSTRACT

A study of optical pattern recognition techniques, available components and new airborne optical systems for use in landmark identification was conducted and achieved promising results. A data base of imagery exhibiting multi-sensor, seasonal, snow and fog cover, exposure, and other differences was assembled. These were successfully processed in a scaling optical correlator using weighted matched spatial filter synthesis.

Distinctive data classes were defined and a description of the data (with considerable input information & content information) emerged from this study. It has considerable merit with regard to the preprocessing needed and the image difference categories advanced. A new optical pattern recognition system suitable for airborne applications was developed, assembled and demonstrated. It employed a laser diode light source and holographic optical elements in a new lensless matched spatial filter architecture with greatly reduced size and weight, as well as component positioning tolerances.

1. INTRODUCTION

In this eight month contract (March - October 1980), the use of optical pattern recognition (OPR) techniques for landmark identification in NASA applications was studied. The three aspects of this program were to: obtain an image data base (typical of image differences to be expected among images), apply OPR techniques to this data, and assess components and architectures for an airborne OPR system for landmark identification. All phases of the work were successfully completed.

The major problem in NASA and other image processing research is that advances in sensor technology have rapidly surpassed the ability of our data processing systems to intelligently process the collected data in a timely manner [1]. Thus, use of OPR techniques with their high speed and parallel processing features appears to be attractive [2].

Our first task was to assemble a representative set of NASA imagery taken of the same area at different times and on different orbits. Our major concern was to maintain pattern recognition (PR) even in the presence of various expected differences among images of the same scene (e.g. seasonal, wavelength, etc. differences). The data base of 78 images assembled is described in Sect. 2.2. From this data base, we selected 25 images that typified nine differences expected among data of the same area (see Sect. 2.3). This selection and moreso the image groupings were finalized after much extensive correlation work was performed. In Sect. 2.4, we note the different image classes and image difference categories finally selected. A brief discussion of the dominant image differences that typify each category is advanced in Chapter two.

A scaling optical correlator using matched spatial filter (MSF) synthesis was assembled to test and evaluate the ability of an OPR system to maintain correlation between the aforementioned image sets with various image differences present. This experimental test bed system is described in chapter three. The OPR techniques applied contribute significantly to image understanding and to the origin of the information and noise content of NASA image data sets with various image differences present.

The results of our experimental optical image PR program are summarized in Chapter 4. In all cases, excellent correlation results with large output correlation peak intensities (I_p) and signal to noise ratios (SNR) were obtained for the various image difference sets examined. A description of the data obtained shows the usefulness of OPR techniques and provides valuable information on the data content and noise content of the data as well as directions for future research.

A summary of available components for an OPR sytsem for NASA landmark identification was also performed. A laser diode was chosen as the light source, holographic optical elements (HOEs) were chosen as the optical elements and a 2-D output CCD detector array was selected. A new optical system using a laser diode source and HOEs was assembled, tested and demonstrated. This system and the excellent correlation results obtained on it are presented in Chapter 5. Our summary and conclusions are advanced in Chapter 6.

REFERENCES

1. D. Casasent, "Coherent Optical Pattern Recognition", Proc. IEEE, May 1979.

2. W. Sivertson and R.G. Wilson, SPIE 202, 17 (1979).

2. IMAGE DATA BASE

2.1 INTRODUCTION

The image data base for this study was obtained by Mr. G. Wilson of NASA Langley. It contains 78 images in sets that demonstrate many of the typical image differences to be expected and on which one must maintain correlation. This data and various NASA references for it are noted in Sect. 2.2. From this imagery, we selected 25 images that typify nine image differences of concern for detailed study. These data are included in Sect. 2.3. This image set selection was made after much of the OPR experiments to be described later (Chapter 4) were completed. The image classes and image difference categories finally chosen are noted in Sect. 2.4. Assembling such a data set was a quite significant effort in itself.

2.2. IMAGE DATA BASE

Two sets of images were received from NASA. Original black and white negative transparencies (approximately 53mm high x 54mm wide) with 3548 pixels per line and 2983 lines per image were obtained from the US Geological Survey. (EROS Data Center). Transparencies 21.5 mm x 22 mm on 35 mm film were also obtained from NASA. These latter images contain four different exposures for each NASA image. The 35 millimeter imagery was used in all of our OPR experiments. These images were collected by the multi spectral scanner (MSS) system on board the Landsat 1,2 and 3 missions. The Landsat MSS systems are line scanning devices that continually scan the earth in a 185.3 km (100 nmi) swath perpendicular to the Landsat orbital track. The Landsat 1 and 2 MSS data provide earth reflected sunlight images in four spectral bands (band four-band seven). The Landsat 3 MSS data contains an additional band (band eight) that provides a thermal infrared radiation image of the scene. The specific spectral response bands used in LANDSAT MSS imagery are listed in Table.2.1.

Each MSS spectral band in Landsat 1 and 2 utilizes six detectors. Bands 4,5 and 6 employ photo-multiplier detectors, band 7 uses a silicon photo-diode to achieve extended infrared response. Band 8 data on LANDSAT 3 used two mercury cadmium telluride detectors. The analog signals from the MSS detectors are digitized and formatted into a 15 megabit/sec data stream for transmission to an earth receiving station or for on-board recording. The received MSS data was further processed by the NASA Goddard Image Processing Facility (IPF) and transformed into frame imagery with an overlap between adjacent frames. Further details on the hardware and processing techniques can be found in reference [1].

Most images received from NASA were recorded in band 5 (0.6 μm - 0.7 μm). Imagery in this band yields more contrast than does band 4 data because of the greater atmospheric influences in the shorter wavelength channel.

2.3 SELECTED IMAGE SETS

A total of 78 images were received from NASA. These covered many different missions, image types, and moreso many expected image differences. Twenty-five images were selected from this data base. These are listed in Table 2.2. The corresponding image numbers in column one are referred to in future experiments. The class of image difference within each of the nine sets of data is also noted in this table, together with the various conditions under which the data were obtained. Representative examples of several of these images are included in Figs. 2.1-2.4.

2.4 IMAGE CONTENT AND CLASSIFICATION

In this section, we describe the image categories and classes selected from the available NASA data in more detail, with attention to general image classes and

TABLE 2.1 SPECTRAL RESPONSE FOR LANDSAT MULTI-SPECTRAL SCANNER (MSS) BANDS.

Band No.	Class. of Information	Wavelength Response (μm)
4	Blue-green	0.5 - 0.6
5	Green-yellow	0.6 - 0.7
6	Red	0.7 - 0.8
7	Infrared	0.8 - 1.1
8	Thermal 1R	10.4 - 12.6

TABLE 2.2 LIST OF IMAGE PAIRS USED IN EXPERIMENTS

CATEGORY	GROUND INFORMATION	SUN ANGLE EL	SUN ANGLE AZ	TIME TAKEN	MSS BAND
Season	Denver area in winter vs. summer				
1.2		22	151	11 Jan 1973	5
2.2		60	118	10 Jul 1973	5
Season	Delaware Peninsula				
7.3	Winter	32	145	13 Feb 1973	5
8.3	Fall	51	133	30 Aug 1973	5
Snow Covered	Lake Tahoe area				
3.2	different amount of	54	131	21 Apr 1973	5
4.2	snow cover.	61	120	27 May 1973	5
Flooding	Mississippi/St. Francis Area.				
9.2	No Flooding	44	143	01 Oct 1973	
10.1	Low Flooding	35	141	22 Feb 1973	5
11.2	Max. Flooding	59	122	05 May 1973	
Fog	Northern California				
12.2	With Fog	25	145	24 Jan 1975	
13.3	Without Fog	41	146	06 Oct 1972	5
Sun Angle	Phoenix area with				
16.3	different sun	60	111	15 May 1974	
17.2	angles.	52	123	31 Aug 1974	5
18.2		31	148	15 Nov 1975	
Exposure	Exposure Difference	Same Sun Angle			
18.1					
18.3		31	148	15 Nov 1975	5
18.5					
Different Spectral Bands	Southern Louisiana in different MSS bands.				
25.3		54	117	16 Apr 1975	4
26.3		54	117	16 Apr 1975	5
27.3		54	117	16 Apr 1975	6
28.3		54	117	16 Apr 1975	7
Different Spectral Bands	California, south of Fresno (Agricultural Valley).				
29.2		46	119	30 Aug 1977	4
30.4		46	119	30 Aug 1977	5
31.4		46	119	30 Aug 1977	6
32.3		46	119	30 Aug 1977	7

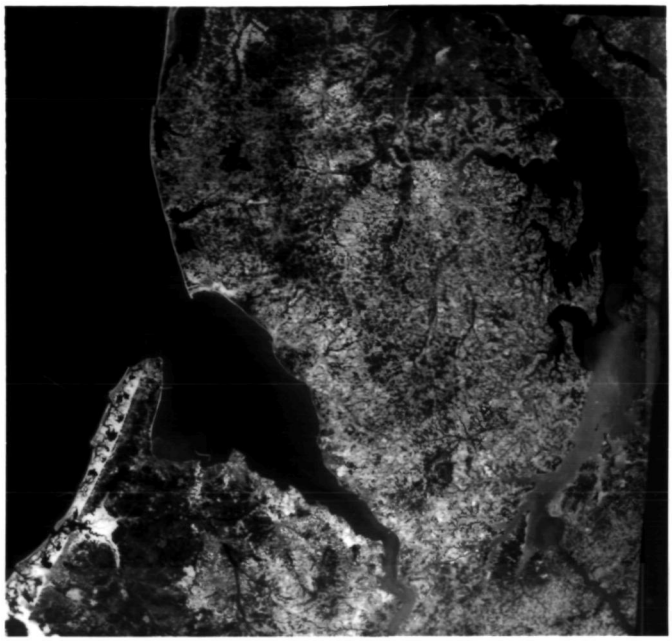

(a) Image 7.3, winter scene.

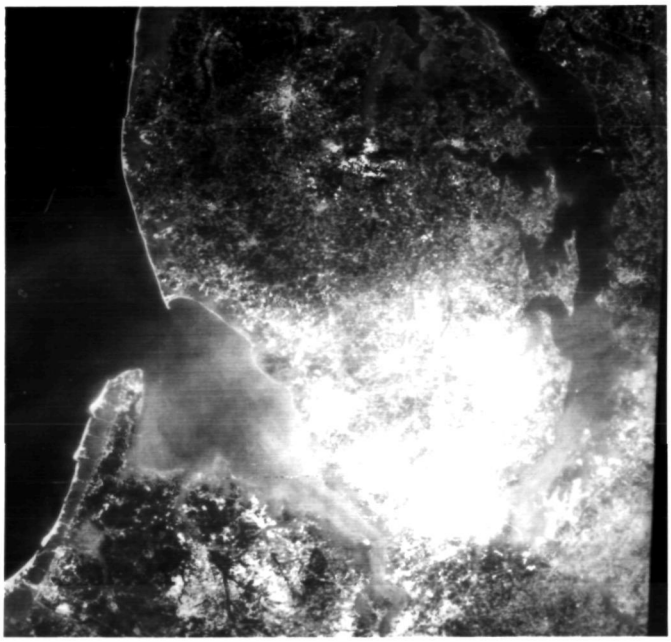

(b) Image 8.3, fall scene.

Figure 2.1 Image set exhibiting seasonal differences.

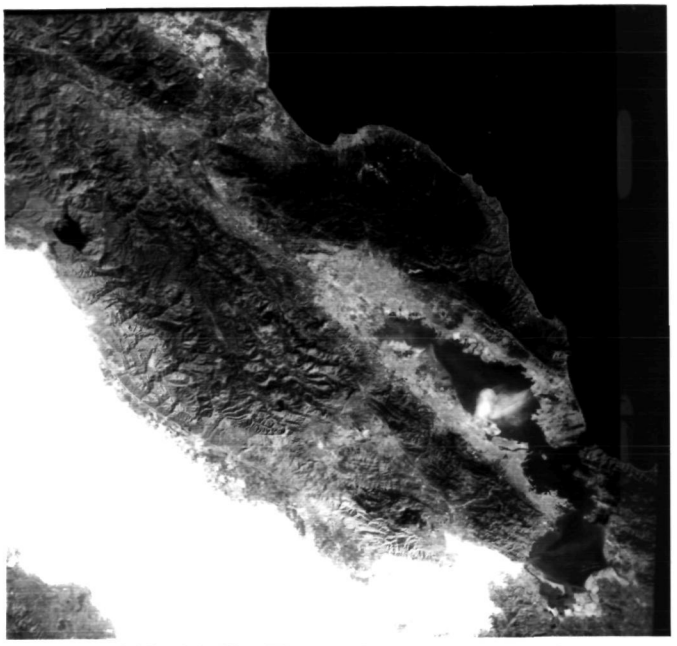

(a) Image 12.2, scene with fog.

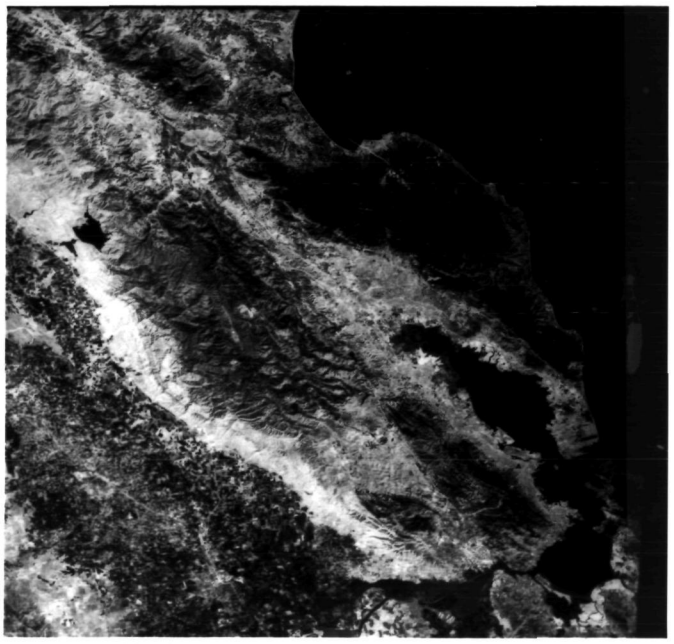

(b) Image 13.3, scene without fog.

Figure 2.2 Image set exhibiting fog cover.

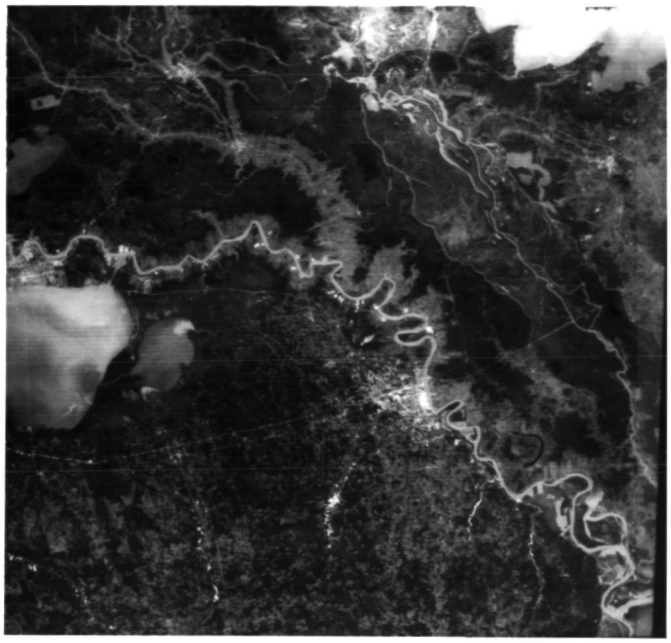

(a) Band 4, image 25.3.

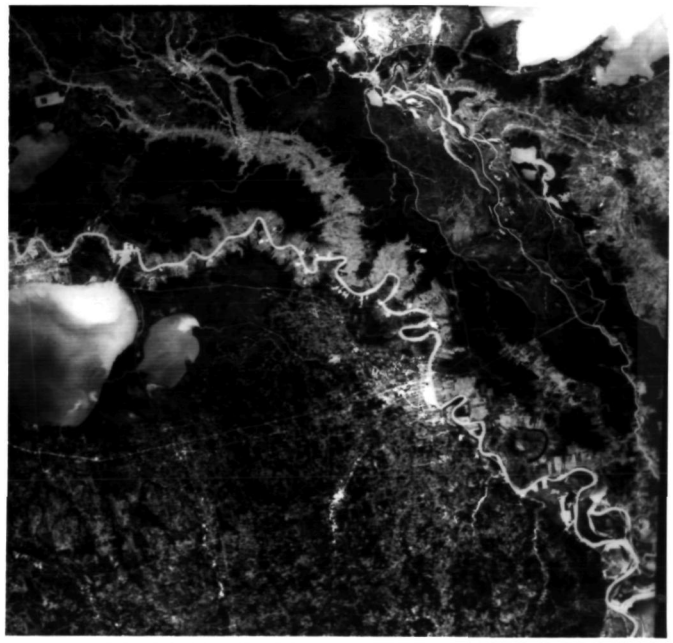

(b) Band 5, image 26.3.

Figure 2.3 Urban imagery taken at different wavelengths.

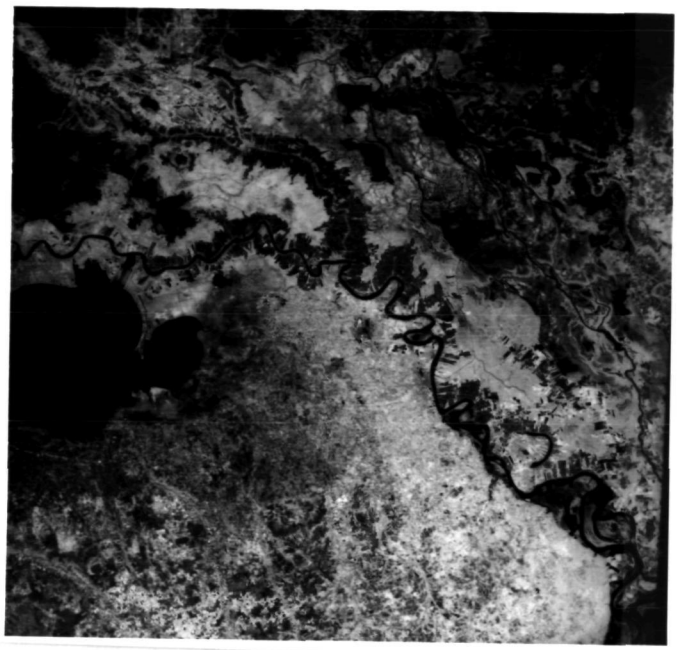

(c) Band 6, image 27.3

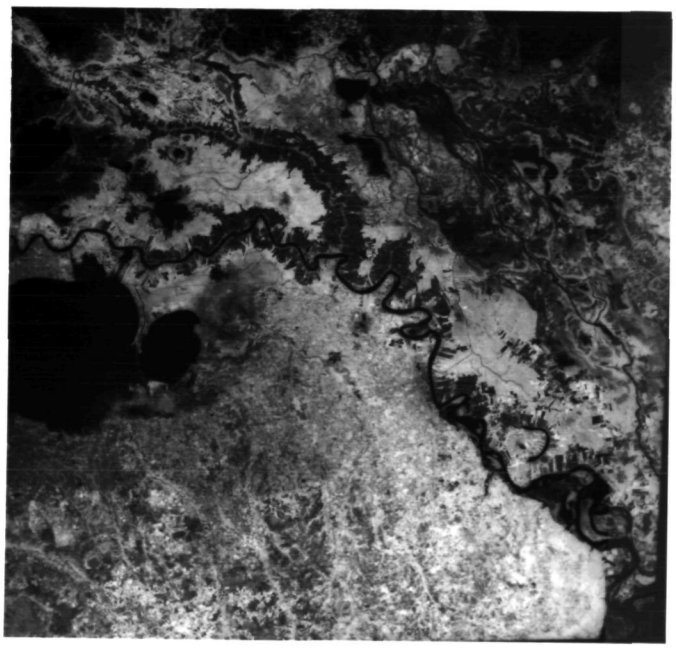

(d) Band 7, image 28.3

Figure 2.3 Continued

(a) Band 4, image 29.2.

(b) Band 5, image 30.4.

Figure 2.4 Rural imagery taken at different wavelengths.

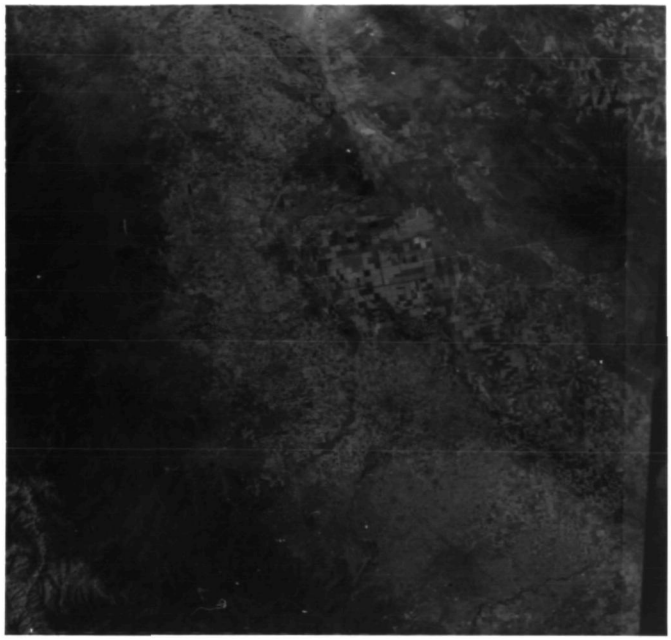

(c) Band 6, image 31.4.

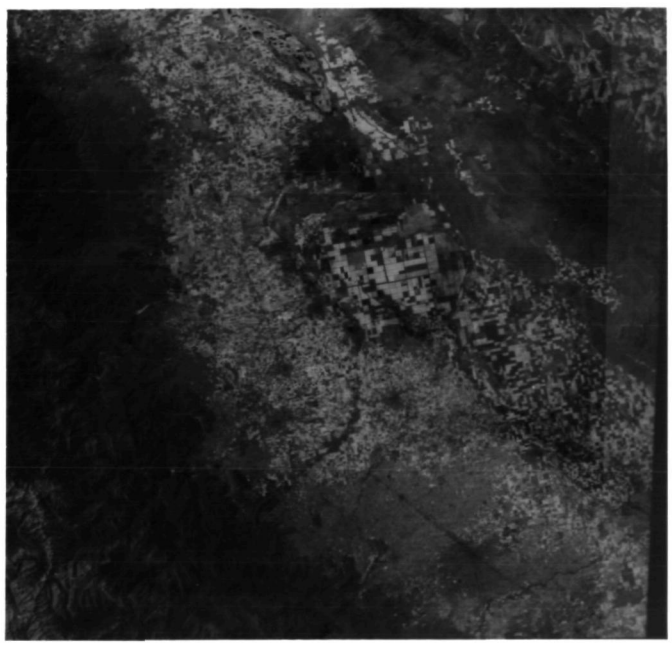

(d) Band 7, image 32.3.

Figure 2.4 Continued

the various image difference categories present. As noted before, these image divisions were arrived at after extensive OPR analysis. The two major classes of imagery selected concern the scene itself. In this area, we chose agricultural and non-agricultural as the dominant image categories, with desert imagery (characterized by little information content) and imagery of mountainous regions (in which geometrical errors due to shadows were of concern) being two minor separate categories. Six types of image differences are described in decreasing order of importance in the following subsections.

2.4.1 Geometrical Errors

Scale, rotation and deformation are the major correlation degradation error sources in two-dimensional pattern recognition. Since the satellite for NASA image acquisition is located at a high altitude (nominally 900 km), we expect quite small scale differences and hence very small scale errors in the resultant data. Rotational differences exist but are also quite small among LANDSAT image pairs, and these errors can be corrected, since the orbit of the satellite is known. The NASA imagery we received had been pre-processed by the IPF NASA facility. The quoted geometrical correction accuracy of the data received was better than one pixel (90% of the time). We therefore do not expect and did not notice any geometrical error in the data base.

Whether the geometrical distortion operations performed on the data can be achieved in real time on board the satellite is an issue of concern that must be addressed in a global overall scenario.

2.4.2 Seasonal Changes

A ground scene observed in different seasons will exhibit different characteristics in reflected sunlight. This change in reflectance is more severe in

vegetation field than in urban imagery. This occurs because there is very little change in the latter case, whereas the reflection of agricultural areas varies quite widely depending on the crop, the sensor's wavelength, etc. If the scene consists of a large number of independent substances (such as vegetation fields, each with a different crop), the resultant sensed scene will display random contrast changes if observed in different seasons. It will also exhibit changes in geometrical shape due to the particular allocation of land use at various times of the year and the reflectance of the various crops. The contrast reversal changes present in such data generally domminated the imagery we observed. Small geometrical differences were also present in this imagery, however this error source appears to be small by comparison to the contrast reversal effect.

This class of image data is very difficult to model. Predicting the changes to be expected with seasonal changes in an image is impossible without a detailed knowledge of the ground scene at the time of the imaging operation. Certain preprocessing techniques can be used to enhance the SNR of the correlation between two such images. These preprocessing operations will be discussed elsewhere.

A winter scene with snow cover or scenes with fog cover are classified as imagery exhibiting data drop-out rather than seasonal changes. This classification was made because the dominant effect in snow-or fog-covered data was found to be removal of the textural information of the scene, and moreso a loss of spatial or modulation data. Hence such data differences are best classified and discussed in Sect. 2.4.5 rather than here.

Urban image correlations are expected to be far less dependent on seasonal differences than are agricultural scenes. Some improvement in correlation performance may be possible by selecting specific wavelengths to use, but this is quite scene-dependent. In agricultural imagery with seasonal differences, the granular

structure of the different crop areas is not visible. Low SNR may result in the appearance of many random contrast reversals. Noise in such correlations arises mainly from the scene's bias level; since this is constant, so is the noise in most such data. The correlation plane signal from such data sets depends on the number of edges in the scene and on the number of independent objects (e.g. fields) in the scene.

2.4.3 Different Spectral Bands

Atmospheric conditions influence the quality of any sensed image. This effect is more severe in the shorter-wavelength region. Thus, higher contrast imagery was generally obtained in band 5 rather than in band 4. In addition to the difference in degree of contrast that such imagery exhibits, contrast reversals are present between the different substances present in the image when they are viewed in different spectral bands. The amount of information change observed depends upon the characteristics of the substances, the atmospheric conditions, and the illuminating wavelength used. Such data is best characterized by contrast reversals than by contrast reduction.

Although the data in various spectral bands are acquired sequentially (within 65μsec for Landsat 1 and 2, within 800 μsec for all five bands in Landsat 3), acquisition is quite fast. It is thus reasonable to assume that no atmospheric change or geometrical error is present during this short period of time. Therefore, the only effect present in such data sets is due to the differences in the spectral responses of the different ground substances for bands 4-7. Only one image exists in the data base for band 8 and it is of quite poor quality. If no geometrical distortions are present, acceptable output correlation peak SNR can be obtained even though the SNR of this input image is quite low.

A secondary result of multi-spectral image correlations is the measure that they provide of image quality and their effect on correlation plane SNR. When few objects are present in a multi-spectral scene, little loss in correlation plane SNR is expected; whereas, when the scene contains many objects, their wavelength reflectance becomes more random. One must, however distinguish (in such remarks) between objects and key or independent objects. A scene can have many objects, most of which are of the same substance and thus all respond the same for a given wavelength. Hence, such an image has few independent objects (i.e., few image regions with independent gray level transmittance values). In general, multi-spectral urban imagery is far less a problem than is agricultural imagery. In the latter case, the general effects of multi wavelength imagery are similar to that present in seasonally different agricultural data.

2.4.4 Diurnal Effects

Although the satellite passes over the same point on the earth at essentially the same local time every 18 days, the lighting conditions for the ground scene change due to the seasonal motion of the sun. The effect is the same as if the same scene were sensed at a different time of the day. This diurnal effect is especially strong in the infrared region (wavelengths longer than .4μm) and is particularly noticeable if the scene contains a water boundary. This occurs because the maximum temperature excursion of water is significantly less than that of other materials surrounding it and water also tends to hold its heat longer than other substances. Thus, terrain temperatures will usually vary from above or below that of water at different times of the day and night. This results in total contrast reversal between images sensed in the day and the night. Among the image file we received, no image pair showed this diurnal effect. It is not expected to be of concern since it dominates near water and in such cases

the scene is classified as one with few key objects and thus the effect is minimal. In other imagery, the effect is more ; a moderate overall contrast change in the imagery rather than random contrast reversals.

2.4.5 Data Drop-Out

Cloud cover, snow cover and flooding can cause certain areas of the scene to be masked out. This results in no textural information in affected area and hence a loss of spatial data. Fog and smoke reduce the intensity of the reflected irradiance from the ground scene and thus result in a loss of image modulation and hence again in a loss of data. Wrong exposure or decreased modulation in recording the data are also considered to be data drop-out effects, since they decrease the SNR of the image.

Cloud or snow cover usually displays some spatial grain structure in the sensed image. We did not observe this phenomenon in our image. The reason may be due to the fact that the fine grain structure was below the smallest resolution element of the data. Another possible reason may have been the low grain contrast compared to that of the surrounding image features. Thus, such image differences result in general in a loss of input data and hence output I_p and SNR.

2.4.6 Sun Elevation Angle

Due to the north/south seasonal motion of the sun, sun elevation angle differences are present even though the images are taken at the same local time but at different days of the year. Changes in sun angle will cause variations in the lighting conditions under which the imagery is obtained. The effect on a given scene is very dependent on the scene itself, but in general results in a shift in the effective wavelength of illumination. This effect is in general quite low and negligible.

Sand is more sensitive to changes in sun angle than most types of vegetation. Because of this scene dependence, each type of scene must be evaluated individually to determine the range of sun angles over which useful imagery will be obtained.

At low sun angle, the greater depth of the atmosphere that the light must penetrate causes the blue portion of the sun's light to be almost completely scattered. Therefore, low sun angle should be avoided in taking imagery.

Geometrical distortion might be observed from the shadow of rough terrain (specifically high mountainous areas) at various sun angle differences. Again, this effect is quite small due to the small angle differences and the fact that the flatter region surrounding the mountains will in general not be affected by such issues.

2.5 CONCLUSIONS

The discussion in this section has raised many important issues concerning the origin of noise, signal content and imagery. In general, image modulation and bandwidth control the information content of an image pair and affect the output I_p and SNR of the correlation. The presence of large uniform image areas is a prime source of correlation plane noise. In our experiments in Chapter 4 and in our recommended pre-processing work, attention is given to enhancing and reducing these different image features.

REFERENCES

1. Landsat Data Users Handbook, US Geological Survey, 1979.

3. OPTICAL PATTERN RECOGNITION SYSTEMS

3.1 INTRODUCTION

In this chapter, the OPR experimental system and techniques used in processing the image difference data sets selected in Chapter 2 are described. In Sect. 3.2, the basic frequency plane correlator OPR system is described. MSF synthesis is treated in Sect. 3.3 and weighted MSF synthesis in Sect. 3.4. The experimental scaling frequency plane correlator system used with weighted MSFs is presented in Sect. 3.5.

3.2 FREQUENCY PLANE CORRELATOR

The use of the coherent optical correlator is well known in performing two-dimensional correlation operations [1]. The classical frequency plane correlator (FPC) or MSF correlator is shown schematically in Fig. 3.1. Plane P_0 is the input plane. It contains the input data (usually in a liquid gate, if film is used as the input media). Plane P_1 is the Fourier transform (FT) plane where the MSF is formed and plane P_2 is the output correlation plane.

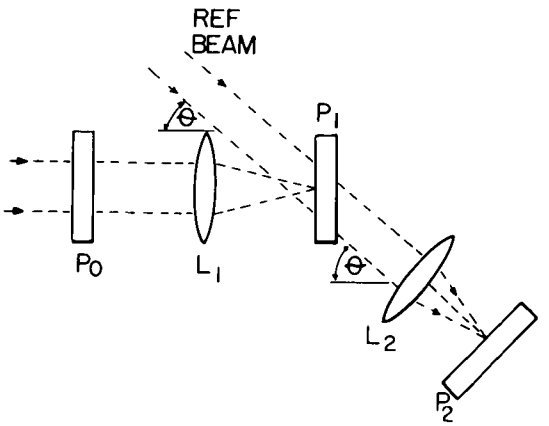

Figure 3.1 Schematic of a frequency plane correlator system.

If the amplitude transmittance of P_0 is $f(x_0,y_0)$ and P_0 is illuminated with coherent light of wavelength λ, then the 2-D Fourier transform F(u,v) of $f(x_0,y_0)$ is formed at P_1 by lens L_1. The spatial frequency coordinates (u,v) in units of cycles/mm are related to the distance coordinates (x_1,y_1) in units of mm in plane P_2 by

$$(u,v) = \left(x_1/\lambda f_{L1},\ y_1/\lambda f_{L1}\right), \tag{3.1}$$

where f_{L1} is the focal length of lens L_1.

With $f(x_0,y_0)$ at P_0, F(u,v) is incident on P_1. If plane P_1 contains an MSF whose transmittance is proportional to $G^*(u,v)$, the complex conjugate of a second function $g(x_0,y_0)$, then the light distribution leaving P_1 is $F(u,v)\ G^*(u,v)$. At P_2 we will obtain

$$R(x_2,y_2) = f(x_0,y_0) \circledast g(x_0,y_0), \tag{3.2}$$

which is the cross correlation function between f and g.

3.3 MATCHED SPATIAL FILTER SYNTHESIS

We now consider how to record the matched spatial filter G^*. If $g(x_0,y_0)$ is placed in plane P_0 and plane P_0 is illuminated by coherent light of wavelength λ, G(u,v) will appear at P_1. A reference planewave illuminates P_1 at an angle and from the same coherent source and with approximately the same path length as the wave traveling through $g(x_0,y_0)$. If the reference beam forms an angle θ with the z axis of the signal path, the total light distribution incident on P_1 is

$$T(u,v) = G(u,v) + R \exp\left(-j2\pi\alpha x_1\right), \tag{3.3}$$

where R is a constant and $\alpha = (\sin\theta)/\lambda$ describes the carrier frequency due to the interference between the signal beam G(u,v) and the reference beam.

The recording material at P_1 is intensity sensitive, usually a photographic plate. After exposure and development, and assuming linear recording, the transmittance of this plate will be proportional to

$$T(x_1,y_1) \propto |G(u,v) + R \exp(-j2\pi\alpha x_1)|^2$$
$$= |G(u,v)|^2 + R^2 + RG(u,v) \exp(+j2\pi\alpha x_1) + RG^*(u,v) \exp(-j2\pi\alpha x_1). \quad (3.4)$$

The last term (3.4) is the desired complex conjugate transform G^* of $g(x_0,y_0)$.

If $f(x_0,y_0)$ is placed at P_0 and the MSF of $g(x_0,y_0)$ is placed at P_1, the light amplitude distribution emerging from P_1 will be given by

$$|G(x_1,y_1)|^2 F(x_1,y_1) + R^2 F(x_1,y_1) + RF(x_1,y_1)\, G(x_1,y_1) \exp(+j2\pi\alpha x_1)$$
$$+ RF(x_1,y_1)\, G^*(x_1,y_1) \exp(-j2\pi\alpha x_1). \quad (3.5)$$

The last term diffracted from plane P_1 will travel along the direction of the planewave $\exp(-j2\pi\alpha x_1)$ and after Fourier transformation by lens L_2, the desired correlation function

$$u(x_2,y_2) = \iint f(x,y)\, g(x-x_2,y-y_2)\,dxdy, \quad (3.6)$$

will appear at the correlation plane P_2, where the integration is over the input aperture of the function to be correlated.

3.4 WEIGHTED MSF SYNTHESIS

By properly setting the ratio of the reference beam to signal beam intensity when making the MSF, we can emphasize the spatial frequency bands recorded on the filter. This weighted MSF synthesis concept [2] is briefly discussed here. We first rewrite the transmittance of P_1 in (3.4) as

$$t(x_1,y_1) = |G|^2 + R^2 + r\,|G| \cos(2\pi\alpha x_1 + \text{Arg } G). \quad (3.7)$$

The exposure incident on plane P_1 is

$$E_1(x_1,y_1) = t(x_1,y_1)\, T$$
$$= R^2T\left[1 + |G|^2/R^2 + 2(|G|/R)\cos\left(2\pi\alpha x_1 + \text{Arg } G\right)\right]$$
$$= E_B\left[1 + 1/K + (2/\sqrt{K})\cos\left(2\pi\alpha x_1 + \text{Arg } G\right)\right], \qquad (3.8)$$

where

$$T = \text{Exposure Time} \qquad (3.9a)$$

$$E_B = R^2T = \text{Bias Exposure} \qquad (3.9b)$$

$$K = R^2/|G|^2 = \text{Beam Balance Ratio.} \qquad (3.9c)$$

The bias exposure E_B and the beam balance ratio K are defined in (3.9). From this final formulation of the transmittance of P_1 in (3.8), we note that the modulation of the data peaks when K = 1. From (3.9) and the observation that G varies spatially with distance x_1 or spatial frequency u in P_1, we see that K and hence the modulation of the MSF data also varies spatially. By weighted MSF synthesis, we mean that we can select the spatial frequency f^* at which K is set equal to one. This gives optimum modulation to a certain band of spatial frequencies centered at f^*.

When the spatial frequency f^* at which K is set equal to one (and hence the spatial frequency at which the modulation is maximum) is chosen to be high, the higher spatial frequencies of the scene are emphasized. Therefore, depending upon the spatial frequency content of the scene, the proper f^* band is chosen in order to ensure optimum SNR value. Weighted MSF synthesis can also be used to control the width of the correlation peak. Setting K = 1 at a higher spatial frequency band records higher spatial frequency components. This results in the recording of a higher band-width on the MSF filter. The resultant effect during the correlation is that a narrow width of the correlation peak will be obtained.

In our experiments, we varied f^* and by observing the peak intensity I_p and SNR of the output correlation, we learned much about the spatial frequency content of an image, the common spatial frequency nature of an image difference pair, the spatial frequency of the noise, the use of high-pass, low-pass and band-pass pre-processing, etc.

3.5 EXPERIMENTAL FREQUENCY PLANE SCALING CORRELATOR

The optical Fourier transform can also be achieved when the input P_0 is placed behind lens L_1. This results in a scaling correlator with an extra degree of freedom in which changing the scale of the FT pattern is possible simply by changing the distance between the input plane P_0 and the FT plane P_1. The scaling correlator results in a more compact optical system, better control over the scale differences between the input and reference, and less stringent requirements on the FT lens L_1. In practice, it is very difficult to reproduce imagery without introducing some scale change. Thus the scaling correlator has a real-time and practical application. The experimental optical correlator system assembled and used is shown in Fig. 3.2. The components used are noted in Table 3.1.

Not shown in Fig. 3.2 are the TV camera and isometric display detector that we used to adjust the MSF for maximum output correlation peak before performing detailed measurements and scans of the output correlation plane with a scanning photometric microscope.

A wedge-ring detector [3] is used to set the reference to signal beam or K ratio [4]. Four MSFs were made for each image using weighted MSF synthesis with K=1 in the four spectral bands f^* indicated in Table 3.2.

TABLE 3.1 COMPONENTS USED IN THE EXPERIMENTAL OPTICAL SCALING CORRELATOR OF FIGURE 3.2

LASER:	Spectra Physics Model 125A, 50 mw HeNe Laser, Tem_{00} Mode, Vertically Polarized
BS:	Jodon Variable Beamsplitter
LPSF:	Jodon Lens Pinhole Spatial Filter, 20X Microscope Objective Lens and 10 μm Pinhole
L1, L2, L3, L4:	Achromatic Doublet Air-Spaced f/5 Lens, Focal Length 760 mm, Broad-band Coated
θ:	Reference to signal Beam Angle, Set Equal to 12.7°
P_0:	Input Liquid Gate Holder (Accepts up to 50 mm x 50 mm inputs)
P_1:	Matched Spatial Filter Plane, Kodak 131 High Speed Holographic Plate
P_2:	Output Correlation Plane
D:	25 x 2500 μm Slit Fiber-Optics Probe
PMT:	Gamma Scientific Photo-Multiplier Tube
PM:	Carnegie-Mellon University Built High Dynamic Range Photometer System
d:	Distance between P_0 and P_1 (495mm)
M:	Front Surface Mirror $\lambda/10$

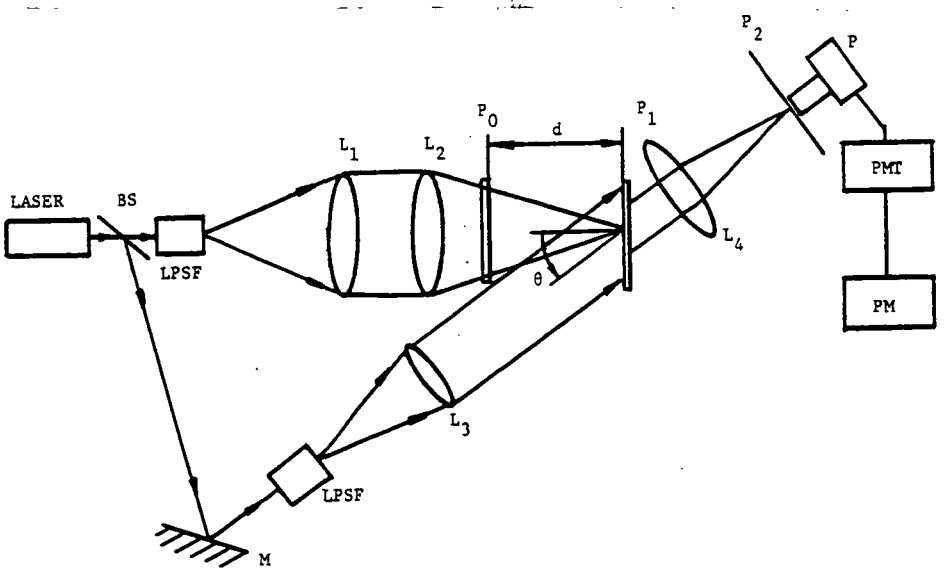

Figure 3.2 Experimental optical scaling correlator system.

TABLE 3.2 MSF FREQUENCY BANDS USED IN FILTER SYNTHESIS

Band	Spectral Frequency cy/mm
A	0.78 - 1.65
B	1.73 - 2.73
C	2.81 - 4.10
D	4.18 - 5.97

The images supplied were 22 x 21.5 mm^2. We apertured a 12 x 13 mm^2 portion of these and used it as the reference image and a larger portion (20 x 20 mm^2) as the input image for all correlation experiments. This procedure avoided the contribution to the correlation peak made by the aperture function. This effect can be large and will manifest itself when the input and reference imagery are in the same sized aperture. Another reason for aperturing only a portion of the reference image was that relative shifts are present between the images of each pair. This procedure ensures that the portion of the image used to make the MSF is within the frame of the other paired input image.

REFERENCES

1. A. van der Lugt, IEEE, IT-10, 139 (1964).

2. D. Casasent and A. Furman, Applied Optics, 15, 1652, 1662 (1977).

3. H. Kasdan and D. Mead, EOSD, 248 (Nov 1975).

4. D. Casasent and A. Furman, Applied Optics, 15, 1690 (1976)

4. OPR EXPERIMENTS FOR LANDMARK IDENTIFICATION

4.1 INTRODUCTION

All of the image sets noted in Table 2.2 of Chapter 2 for the various image difference classes were correlated using the OPR system described in Chapter 2. The results of this lengthy experimental effort are summarized in Table 4.1. For each of the nine image difference classes noted, MSFs of different images were made with different f^* bands. For each case, the peak intensity I_p and the SNR of the output correlation plane pattern were measured and used as the system's performance measures. These data are included in Table 4.1. In total, over 300 MSFs were synthesized and 800 correlations were performed: four MSFs with different f^* and four different exposures for each of the 25 image difference pairs. Most of the experiments were performed by using 649F MSF plates and then repeated by using HSH 131 MSF plates. The shorter exposure time needed with the HSH plates provided the more reliable results that are included in Table 4.1.

It should be noted, as shown in Table 4.1, that excellent correlation results were obtained for all image difference sets and image difference pairs investigated. This shows the use of OPR techniques and weighted MSF synthesis in landmark identification for this NASA data base. In this chapter, we consider these correlation data in more detail to obtain further insight into the reasons for the results obtained. This effort will provide us with necessary information on the origin of signal and noise in such landmark identification cases and this should agree with the different image content issues advanced in Chapter 2. This study should also lead to signal and noise models for different image differences and image classes and thereby to an overall pattern recognition scheme for landmark identification, while also providing us with input on the optimum image pre-processing operations needed.

TABLE 4.1 EXPERIMENTAL RESULTS OF CORRELATION I_p AND SNR

Category	Correlation Pair		Correlation Peak Intensity I_p At Different f*				Correlation SNR In Different f* (in dB)			
	Filter	Input	A	B	C	D	A	B	C	D
Exposure	18.2	18.1	65	65	62	51	23	24	23	16
	18.2	18.3	67	69	64	56	23	26	23	19
	18.2	18.5	63	66	61	52	18	22	19	14
Season	1.2	1.2	61	67	66	68	16	20	19	22
	1.2	2.2	57	60	62	59	12	12	14	13
Season	7.3	7.3	55	58	59	59	17	19	18	20
	7.3	8.3	50	48	50	47	14	13	11	11
Snow Cover	4.2	4.2	65	70	70	69	18	22	24	20
	4.2	3.2	59	59	60	55	9	11	15	12
Flooding	9.2	9.2	70	72	72	67	24	25	27	24
	9.2	10.1	61	63	64	60	16	19	21	17
	9.2	11.2	66	64	63	61	20	17	19	18
Fog	13.3	13.3	52	55	50	51	13	13	9	10
	13.3	12.2	44	48	45	46	8	10	7	8
Sun Angle	18.2	18.2	67	67	64	56	24	25	24	20
	18.2	16.3	61	61	55	42	18	18	13	6
	18.2	17.2	62	58	52	41	19	15	10	5
Different Spectral Band (Total Contrast Reversal)	26.3	25.3			56				19	
	26.3	26.3			56				18	
	26.3	27.3			55				16	
	26.3	28.3			57				17	
Different Spectral Band (Random Contrast Changes)	30.4	29.2			54				16	
	30.4	30.4			65				25	
	30.4	31.4			46				6	
	30.4	32.3			56				16	

In Sects. 4.2-4.8, data for the various image difference cases noted are described and the experimental results obtained in Sect. 4.1 are explained in terms of the image content issues advanced in Chapter 2.

Again, the excellent correlation plane data obtained show the use of the OPR technique. This was our major purpose. The following discussion and analysis is intended to present more detail on why the indicated performance was obtained.

4.2 EXPOSURE DIFFERENCES (ROW 1 OF TABLE 4.1)

For all of the 35-mm NASA imagery, four different image exposures were available. These effective exposure differences were thus the first image difference considered. For this case, we chose the four exposures of scene 18 (Table 2.2 and Table 4.1). Selection of different exposures for all imagery in each of the data sets was necessary and hence this initial study was conducted first. The numbers from 1-5 after the period in the various image number codes in Tables 2.2 and 4.1 correspond to the different exposures chosen.

Exposure differences result in differences in the average transmittance and the modulation level of the image. To quantify the effects of exposure differences, we thus first measured the amplitude transmittance and the amplitude modulation of the different images of scene 18 with different exposures. The intensity transmittance τ of each image was determined by measuring the dc value of the Fourier transform of the scene. A 22 x 22 mm^2 region of the image was illuminated with helium neon laser light in a converging Fourier transform system with the input plane spaced 495 mm from the Fourier transform plane. The diameter of the dc spot in the Fourier transform pattern for this system is

$$w = 2\lambda d/D = 2(0.63\ \mu m)\ 495\ mm/22\ mm = 28.3\ \mu m. \qquad (4.1)$$

A circular fiber optic detector of effective diameter 50 μm/2.5 = 20 μm was interfaced to a PMT system and used to measure the dc light intensity in the Fourier transform plane. The film density functions D_1 and D_2 (log scale) were measured with and without film in the input, but with a liquid gate in place in both cases. The average film density $D = D_1 - D_2$ was then obtained and from it the film's intensity transmittance $T_i = 10^{-D}$ and its amplitude transmittance $T_a = \left(T_i\right)^{1/2} = 10^{-D/2}$. These data are noted in Table 4.2 for different exposure images of scene 18.

The different image modulation values obtained for different exposure images were also measured from selected cross-sectional scans of edges in the image sets by using a scanning photometric microscope system. The measured intensity differences of an average image edge were converted to amplitude differences by taking the square root of the maximum and minimum intensity readings. The largest amplitude difference was set to a relative modulation of one with lower amplitude differences having correspondingly less relative amplitude modulation. These cross-sectional scan measurements were repeated for each different exposure image of scene 18 with care made to scan the same typical image edge in all images. These data are included in Table 4.2.

MSFs of image 18.2 were made with four different f^* setting and correlations were performed with input images 18.1, 18.3, and 18.5. The I_p and SNR of all correlations were measured, as well as the correlation plane noise for all 12 MSFs with different f^* settings. This extensive experimental analysis provided considerable data on information content and image noise as well as on the effects of exposure differences. As shown in Table 4.2, exposure differences manifest themselves as differences in amplitude transmittance and differences in amplitude modulation of the scene. We expect imagery with larger amplitude modulation to result in more MSF diffraction efficiency and hence in more output correlation plane light and thus

TABLE 4.2 EFFECT OF EXPOSURE DIFFERENCES ON I_p AND SNR

Correlation Pair		Amplitude Transmittance	Amplitude Modulation	I_p				Cross Correlation Noise (dB)				SNR (dB)			
Filter Made	Input Image			A	B	C	D	A	B	C	D	A	B	C	D
18.2	18.1	0.22	0.68	65	65	62	51	42	41	39	35	23	24	23	16
18.2	18.3	0.50	1.0	67	69	64	56	44	43	41	37	23	26	23	19
18.2	18.5	0.75	0.79	63	66	61	52	45	44	42	38	18	22	19	14

a larger I_p output. We also expect larger modulation and diffraction efficiency to contribute more to the signal correlation than to the noise level in the output correlation plane. The data in Table 4.2 shows these trends. Image 18.3 has the largest modulation and thus yields the largest I_p. Images 18.1 and 18.5 have less modulation with nearly equal modulation values for both scenes. The resultant I_p values are less than for image 18.3 and comparable for images 18.1 and 18.5.

The average transmittance level of the image affects the correlation plane noise level in cases where large uniform areas are present in the input scene. This is due to undiffracted light not being totally blocked at the MSF plane and to low-frequency scatter. The exposure data of Table 4.2 verifies the dependence of correlation noise on the average image transmittance. Image 18.5 has the largest T_a value and exhibits the largest correlation plane noise level, etc. The correlation SNR data shows the combined effects of larger I_p (due to larger modulation) and larger noise level (due to larger T_a).

In general, we can say that higher modulation gives higher I_p and higher T_a gives a higher noise level and thus the optimum image bias level or exposure should be chosen to maximize correlation plane SNR. In Fig. 4.1, we show I_p, noise and SNR in units of dB versus f^* for the different exposure images of scene 18.

4.3 SEASONAL CHANGES (ROWS TWO AND THREE IN TABLE 4.1)

The two pairs of images (1.2-2.2) and (7.3-8.3) were chosen to study seasonal changes in an urban image area.. This kind of image contains higher spatial frequencies. The result is an auto-correlation I_p that is best at higher f^* band choices.(band D or higher). Since there are differences between images in different seasons (winter versus summer in image set 1.2-2.2 and winter versus fall in image set 7.3-8.3), the cross correlation I_p will be reduced and the highest I_p will occur

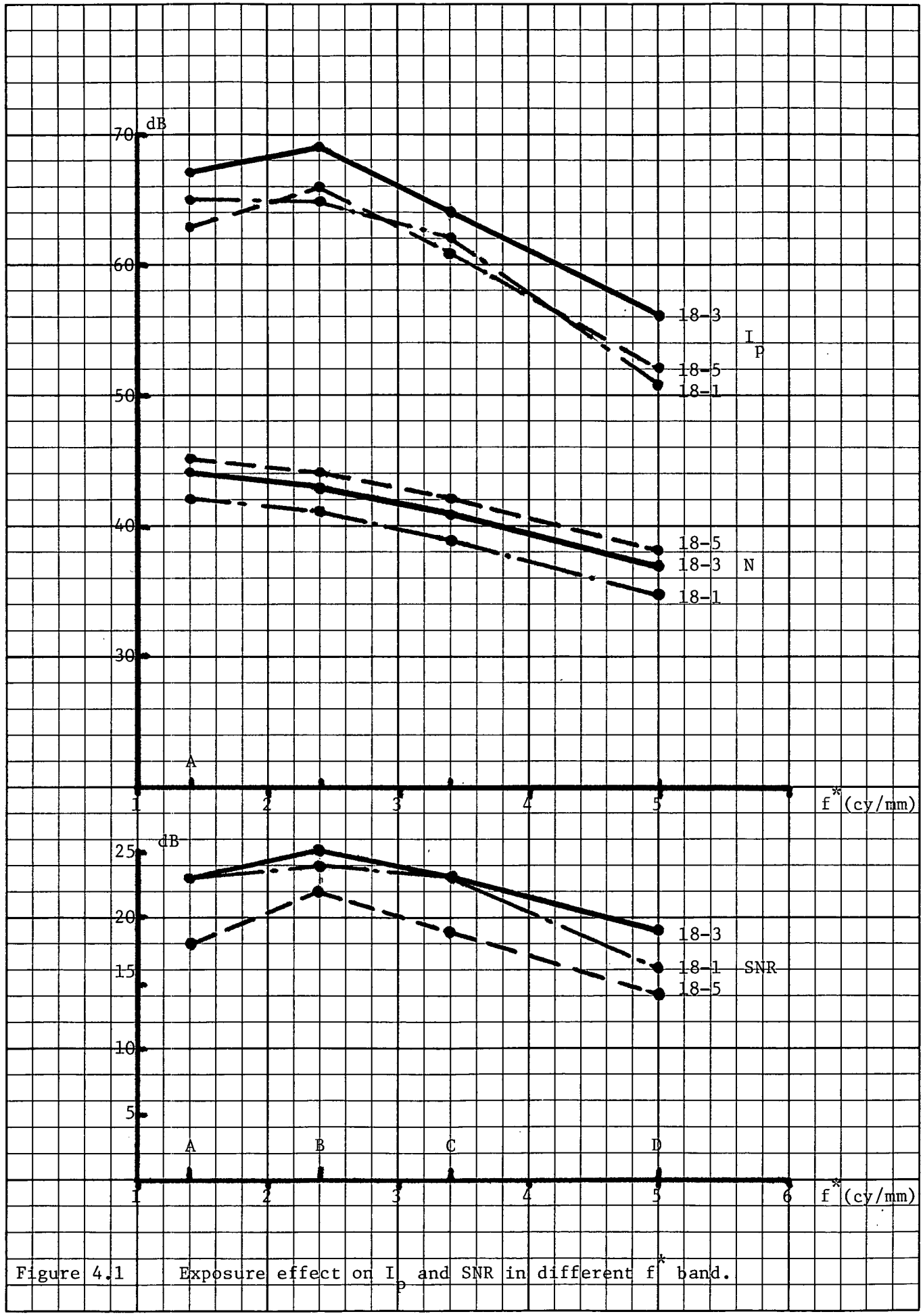

Figure 4.1 Exposure effect on I_p and SNR in different f^* band.

at a slightly lower f^* band. The shift to the best cross-correlation at band C for the 1.2-2.2 case and band A for the 7.3-8.3 case demonstrate these trends. The I_p loss is a measure of the amount of common image information lost due to seasonal differences. The f^* band used is a measure of the spatial frequency region in which this common information lies. The shift to lower f^* bands for cross-correlations indicates that noise (any differences between the two images) for such image sets occurs at high spatial frequencies.

4.4 SNOW COVER (ROW FOUR IN TABLE 4.1)

The image pair 3.2 and 4.2 show the same scene with different amounts of snow cover, with 4.2 having less snow cover than 3.2. The image area is mountainous terrain and therefore there are not many common high spatial frequency components. The auto correlation peak I_p occurs at a lower f^* band C (than for the seasonal auto correlations in Sect. 4.3, for which the auto-correlation peaked in band D). It is interesting to see that the cross-correlation I_p occurs at the same f^* band as for the auto-correlation. This suggests that there are no geometrical differences between images due to different amounts of snow. One reason that we observe no spatial frequency difference between auto and cross-correlations is that the images are taken within the same season and only about one month apart. This is in contrast to the seasonal image pair in Sect. 4.3 for which the images were taken six months apart. The loss in cross-correlation peak intensity and SNR observed for the snow cover is due to the data loss of the scene or to data-drop out effects in those image areas covered by snow. There appears to be a uniform decrease of data over all spatial frequencies, with data loss not concentrated in one spatial frequency band and not in high information bands, such as band C. In some instances, snow can enhance the contrast difference between regions and result in a higher data modulation, but such an effect is a quite isolated occurrence and does not appear in any of the NASA imagery available.

4.5 FLOODING (ROW FIVE IN TABLE 4.1)

Images 9-11 show the same scene containing a river with different amounts of flooding present. Image 9.2 shows the river without flooding. In images 10.1 and 11.2, flooding is present with 10.1 showing more severe flooding than 11.2. This is another example of data drop-out or loss of common image information. We expect the cross-correlation I_p to be higher for the correlation of 11.2 with 9.2 than for 10.1 with 9.2 since the flooding in 10.1 covers a wider area and its effect is a larger loss of spatial data. The experimental data in Table 4.1 verifies these trends. From the 35 mm roll imagery, there are only three exposures taken of image 10 while there are five exposures for image 11 and four exposures for image 9. The exposures for image 10 are generally slightly under exposed. This results in higher T_a and lower contrast than for image 10.1. These combinations of data drop out and exposure differences make exact quantification of the results obtained quite difficult. The experimental results show a lower noise level for the correlation of images 10.1 and 9.2. This makes the resultant correlation plane SNR values of the data closer than one would expect for the 10.1-9.2 and 11.2-9.2 cross-correlations if the only image differences were due to the different degrees of flooding present.

4.6 FOG COVER (ROW SIX IN TABLE 4.1)

Images 12 and 13 are of the same scene with different amounts of fog cover present. The scene is of mountainous terrain and thus contains lower spatial frequency data than do other imagery. Although the image pair were taken more than two years apart, there is still a sizable cross-correlation SNR. Again no shifting in the f^* band occurs in the cross-correlation I_p distribution. This suggests that the major reason for the drop in I_p is due to the fog cover present in image 12.2 and absent in the other image.

In this and the other examples of data drop out (due to snow, modulation decrease, flooding, etc.), the loss in I_p between an auto and a cross-correlation was proportional to the amount of input information loss and this in turn is in general proportional to the input image area (spatial) with drop-out or decreased modulation.

4.7 SUN ANGLE DIFFERENCES (ROW SEVEN IN TABLE 4.1)

Images 16, 17 and 18 are of the same scene taken at different sun angles. More precisely,images 16.3, 17.2 and 18.2 are all taken at different seasons (spring, summer and fall respectively). This effect is analogous to sun angle differences as noted in Chapter 2. It is difficult to analyze the effects of sun angle alone. However, from the experimental auto and cross-correlation results obtained on these images, we see that again a quite large output cross-correlation SNR can be obtained. The drop in cross-correlation peak values appears to be due to contrast changes in the vegetation field in the area due to the change in seasons. As noted in Chapter 2, this type of image difference does not appear to be of major concern in an OPR correlator. The experimental data of Table 4.1 verifies these remarks.

4.8 DIFFERENT SPECTRAL BANDS (ROWS EIGHT AND NINE IN TABLE 4.1)

A recorded image depends on many factors. The irradiance of the sun, the atmospheric condition and the reflectance of the surface all have important effects on the final image. For the case of images of the same scene obtained in different spectral bands, we can classify the data into three different categories:

A. No Contrast Change

B. Total Contrast Reversal (Image Groups 25.3, 26.3, 27.3 and 28.3)

C. Random Contrast Change (Image Groups 29.2, 30.4, 31.4 and 32.3).

The type A multi spectral images occur when the ground scene is a desert, mountain, or urban scene. In such imagery, only the reflectance of the ground varies in intensity as the illuminating wavelength is varied and most important no contrast changes occur between neighboring regions of the image. Therefore such an image pair will exhibit different intensity levels at different illuminating wavelengths, but because of the nature of the content of the scene (few independent objects), contrast reversals are not dominant, rather only differences in input data modulation occur.

The type B images occur when the image contains lakes, rivers and forests or some mountains. In such data, the scene again contains only a few independent objects, with the river, etc. regions being the major ones. Because of the issues noted in Chapter 2, multi-spectral images of such a scene exhibit nearly total contrast reversal. This effect is particularly apparent between band 5 (0.6-0.7 μm) and band 6 (0.7-0.8 μm) multi-sensor images. In general, the cross-correlation of images that are totally contrast-reversed versions of one another perform identically to an auto-correlation and thus represent no problem.

The type C images occur when the scene contains agricultural data in which different crops have been planted next to each other. Since the reflectance of crops at different wavelengths varies from crop-to-crop and from wavelength-to-wavelength, changing the illuminating wavelength results in a random change in contrast between neighboring points of the scene. Such random contrast reversals are a major problem and error source in image difference correlations.

Fig. 4.2 shows a graphical illustration of the three types of images. For simplicity, we consider only data with two intensity levels (one or zero). f(x) is the reference function obtained at a particular wavelength. Total contrast

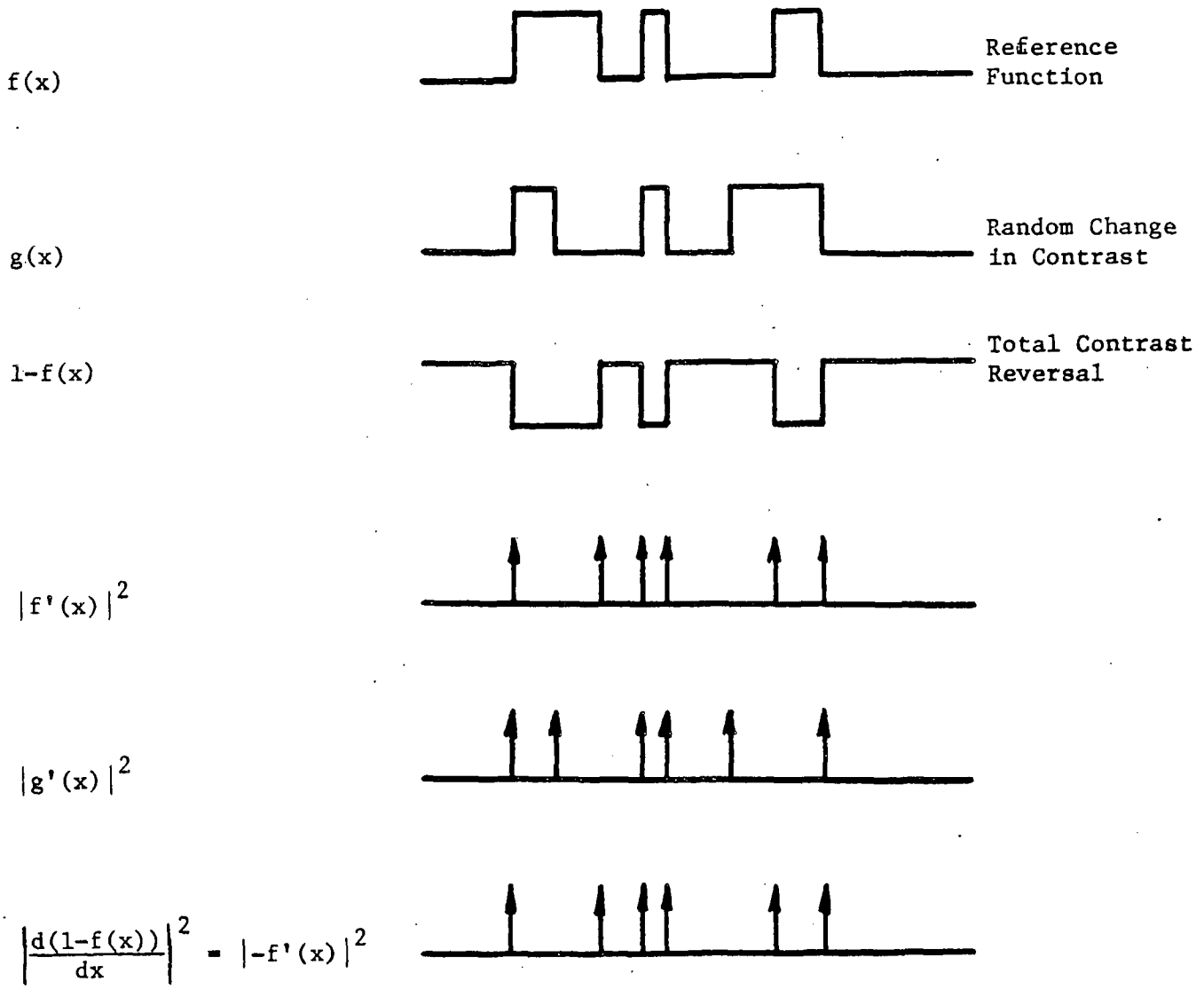

Figure 4.2 Graphical illustration of function that has contrast change.

reversal is shown by 1-f(x) and random contrast change by g(x). If we take the square of the derivative of these three functions, we obtain a display of delta functions in which only edges occur and the magnitude operator has equalized the polarity of the delta functions describing the edges of the image.

As seen in Fig. 4.2, $|f'(x)|^2$ is the same as $|-f'(x)|^2$. Therefore, we expect no loss in information from the total contrast reversal scene. For the case of random contrast changes, only those delta functions that align withthe reference delta functions will contribute to the correlation I_p. Therefore, we expect a drop in cross correlation I_p. The amount of I_p loss depends upon the number of edges that are common between images. In such multi-spectral cases, use of a non-linear magnitude operator unifies the polarity of all image edges and thus enhances the SNR and I_p of the cross correlations. These examples in Fig. 4.2 in the above discussion show the type of pre-processing necessary to enhance cross-correlations for landmark identification.

The experimental results shown in rows 8 and 9 of Table 4.1 verify the above remarks. For the total contrast reversal case, the I_p and SNR values for auto and cross-correlations remain quite close to each other. For the random contrast change case, the largest correlation loss occurs when image 31.4 (MSF band 6) is cross-correlated with the MSF made from image 30.4 (MSF band 5). The resultant SNR value of only 6 dB is the result of the lower overall contrast of the image and the contrast reversal changes that occur when going from band 5 to band 6.

In optical experimental systems, it is not easy to include the magnitude operation shown in Fig. 4.2. When such an operation is included as pre-processing, considerable improvement is expected in the correlation performance of multi-spectral data.

4.9 SUMMARY AND CONCLUSION

In this chapter, we have detailed the highlights of our experimental OPR correlation program on the NASA image difference data base. The results were very promising. We were able to correlate all image difference sets quite well and with good output correlation plane SNR and I_p values in all cases. The tests and discussions in this chapter and the general image content and image classification remarks advanced in Chapter 2 provide a quite acceptable first-level description and explanation of the data base and the image difference problems present. The experimental results in general verify these remarks. Several noise models and signal models involving image area and modulation were suggested and appear to adequately explain the results obtained. For several of the image difference sets, pre-processing is necessary to decrease the magnitude of the output correlation plane loss and to provide a single more unified processor architecture. Quite simple pre-processing operations appear adequate to handle the image difference cases addressed thus far.

CHAPTER 5

A LASER DIODE/HOE PATTERN RECOGNITION SYSTEM

5.1 INTRODUCTION

A compact and rugged optical correlator is described. It employs a lensless matched spatial filter that is formed at one wavelength. Correlation is performed with a laser diode at a second wavelength by using an imaging lens in a scaling correlator topology.

Optical pattern recognition by matched spatial filter (MSF) correlation [1] is a well-known technique. The advent of holographic optical elements (HOEs) [2-3], laser diode sources and new architectures has made rugged and compact versions of such systems very attractive [4-7]. Such systems are useful for both commercial and airborne applications. In this paper we provide the first full discussion unifying all aspects of a laser diode/HOE system. Theoretical analyses, experimental data and the results of several correlations performed on the system are provided.

The system topology we choose uses a lensless MSF [8-9], in which the MSF and the transfer function for the second Fourier transform lens (as an HOE) are combined on a single plate. This results in a rugged system in which critical alignment of these two components is not necessary, as it is in the conventional system. An analysis of this element is provided in Sect. 5.2, with attention to system design, aberrations and the system's shift invariance. A correlation on text data is included and analyzed to show the use of weighted MSF synthesis [10] in reducing the aberration effects of an HOE.

In Sect. 5.3, we consider use of a lensless MSF (formed at one wavelength by using a continuous gas laser) in a correlator using a laser diode source emitting at a different wavelength. A scaling correlator topology that only requires the first lens to image is used in this processor. As a prelude to this system, a lensless MSF was formed at λ_1 = 488 nm and correlated with λ_2 = 633 nm using two different continuous gas lasers. An aberration analysis, system design issues and experimental correlation data are presented for this system.

In Sect. 5.4, we discuss many specific laser diode error sources (including their temporal and spatial coherence) and how they effect such a processor. We conclude with several examples of optical pattern recognition performed on a laser diode/lensless MSF system.

A conventional HOE lens can be produced as shown in Fig. 5.1a by interference of a plane wave reference beam R and the diverging spherical wavefront from a point source. During reconstruction, only wave R is usually present and the HOE thus reconstructs the point source by focusing the plane wave R to the

right of the HOE. In practice R can be either a parallel or diverging beam. It is also possible to rotate the HOE by 180° between synthesis (Fig. 5.1a) and use (Fig. 5.1b). When this rotated HOE is now reilluminated with R, the beam R_- is effectively its conjugate R^* with respect to the HOE. The remaining optical system is unchanged and the point image will now be formed on the original optical axis as shown in Fig. 5.1b.

The main concerns with an HOE lens are its diffraction efficiency η and its optical quality. To maximize η, the intensities of the two beams are adjusted for optimum exposure of the HOE plate (a bias amplitude transmittance of 0.5) and their intensities are set equal (for maximum modulation of the recorded fringe pattern). In practice the η value obtained will be slightly less than the theoretical maximum η = 6.25% value for an amplitude hologram. Under or over-exposure will cause the drop of diffraction efficiency from its optimal value. In our HOE work, 649-F type plates were used for HOE recording. At λ = 633 nm, a total exposure of 80 $\mu J/cm^2$ resulted in $\eta = \sim 3\%$.

Spherical aberration is the optical quality parameter of major concern in an HOE, since the image of the HOE we use is a single point. The quality of such an HOE can be measured from either the deformation of the wavefront leaving the HOE or the intensity distribution in the image plane. Since our HOE is intended for use in a correlator, we chose SNR of the output Fourier transform (FT) produced by the HOE as the measure to be used. We have obtained 55 dB SNR values with an HOE and comparable performance (57 dB) with a conventional glass FT lens for the same simple square and circular input functions. In the lensless MSF we describe in Sect. 5.2, the MSF and HOE are combined. For this

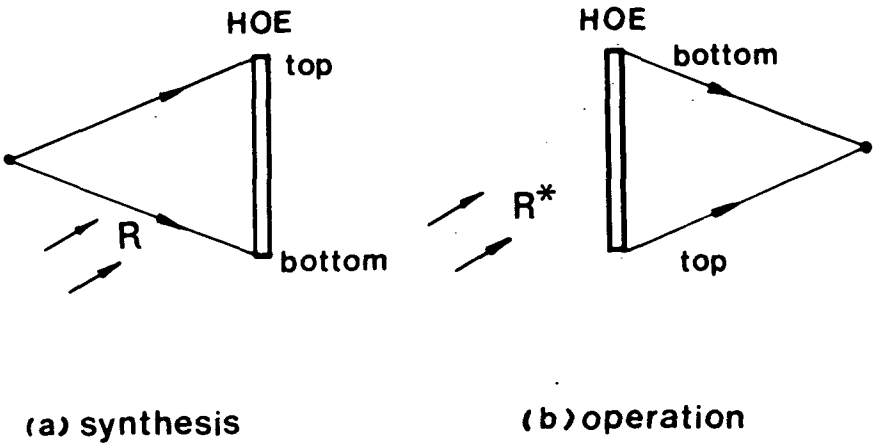

Synthesis (a) and use (b) of a conventional HOE lens.

Fig. 5.1

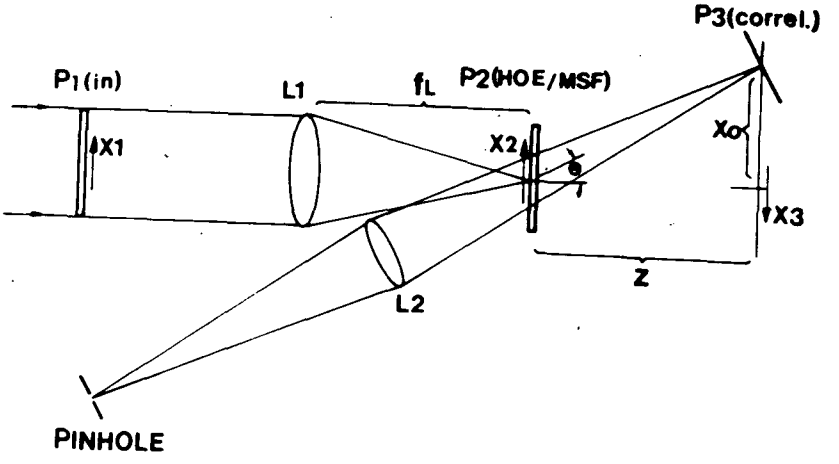

Schematic diagram of a lensless MSF optical correlator system [18].

Fig. 5.2

case, bandpass spatial filtering occurs and HOE aberrations are greatly reduced over those of a conventional HOE (see Sects. 5.2 and 5.4).

5.2 LENSLESS MSF

5.2.1 THEORY

The system used to record a lensless MSF is shown in Fig. 5.2. It is similar to the conventional technique [1] except that a converging reference beam is used rather than a plane wave. For this system, the reference object h(x) is placed at P_1 during synthesis of the MSF. For simplicity of notation, only a 1-D analysis is included, with no loss of generality. The signal beam incident on P_2 is the Fourier transform (FT) of h or $u_s(x_2) = H(x_2/\lambda f_1)$. The spatial coordinates of P_1, P_2, and P_3 are denoted by x_1, x_2, and x_3 respectively; λ is the wavelength of the incident light and f_L is the focal length of lens L_1. The converging reference beam at P_2 is decribed by

$$u_r(x_2) = \exp[-jk(x_0-x_2)^2/2z], \tag{1}$$

where $k = 2\pi/\lambda$, x_0 is the distance from the axis in P_3 at which the converging beam focuses, and z is the orthogonal distance from P_2 to P_3. The pattern recorded at P_2 is $|u_s+u_r|^2$ and we assume that the transmittance of P_2 after development is equal to the incident exposure. The term of interest in this MSF at P_2 is

$$u_t(x_2) = H^*(x_2/\lambda f_L)\exp[-jk(x_0-x_2)^2/2z], \tag{2}$$

where the constant phase factor that described the direction of propagation of this term is omitted for simplicity.

If P_2 is re-illuminated with u_s, then the reference beam will be reconstructed, and in this case a point of light will appear at $x_3 = x_0$. Our major concern is that this occurs without the need for a second FT lens between P_2 and P_3. This is possible, since $u_t(x_2)$ contains both the conjugate FT of h (the MSF) and the transfer function of a FT lens. Moreso, if h is shifted in P_1 during reconstruction, the location of the point of light in P_3 will shift from its original x_0 location by an amount proportional to the shift of h in P_1. This is the shift invariance required in pattern recognition.

To see the use of such a system for pattern recognition, we block the converging reference beam in Figure 5.2 after synthesis of the filter, rotate the HOE by 180^o, and place the input function $f(x_1) = h(x_1+\epsilon) + g(x_1)$ at P_1. This function contains the reference $h(x_1)$ displaced from the origin by an amount ϵ, where $g(x_1)$ denotes the rest of the input. We assume $g \textcircled{*} h = 0$, where $\textcircled{*}$ and * will denote correlation and convolution respectively. For the term of interest in f, the light distribution incident on P_2 is

$$u_2(x_2) = H(x_2/\lambda f_L)\exp(jkx_2\epsilon/f_L). \tag{3}$$

Leaving P_2, we have

$$u_2(x_2)u_t(x_2) = H(x_2/\lambda f_L)H^*(x_2/\lambda f_L)\exp(-jkx_2^2/2z)\exp[jkx_2(\epsilon/f_L+x_0/z)], \tag{4}$$

where constant phase terms have been suppressed for simplicity. Propagation of this pattern from P_2 to P_3 yields a pattern at P_3 that (except for a quadratic phase factor, that is negligible when intensity is detected at P_3) is the FT of (4). Thus, at P_3, we obtain

$$u_3(x_3) = h(x_3 f_L/z) \circledast h(x_3 f_L/z) * \delta(x_3 + x_0 + \varepsilon z/f_L). \quad (5)$$

Inspection of (5) shows that the output P_3 pattern is the auto correlation of h and that it is displaced from the reference point x_0 by an amount $z\varepsilon/f_L$ that is proportional to the displacement ε of h from the center of P_1.

The major feature of this MSF system is that the use of a convergent reference beam enables both the MSF and the transfer function of the correlation lens to be recorded on the same plate at P_2. This decreases the length and complexity of the system plus the number of optical components necessary. Moreso, it provides a more rigid system with no positional tolerances from P_2 to P_3. Many authors have proposed (and some have used) convergent reference beams for diverse purposes including replication of coherent objects without highly corrected lenses [11], synthesis of a multiple filter bank in a noncoherent processor [8], character recognition [9,12], image restoration [13], and for achieving shift-invariance from the point of view of the vignetting apertures [9]. Our concern in this section is: the design and fabrication of a lensless MSF correlator; the use of weighted MSF synthesis [10,14] to control system performance and the aberration effects of the HOE; and the analysis and experimental verification of the shift-invariance of the system.

5.2.2 EXPERIMENTS

The system of Fig. 5.2 was assembled using: λ = 633 nm, f_L = 500 mm; $\theta = 11.3^\circ$ and x_0 = 78 mm. The input function f used is shown in Fig. 5.3a. It contains four occurrences of the key work "PROFESSOR", which we select as our reference function h (Fig. 5.3b). A lensless MSF of this function h was produced at P_2.

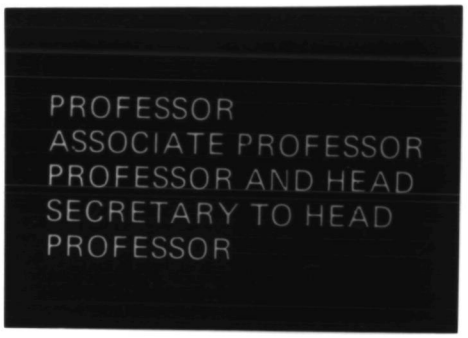

(a) input

(b) reference

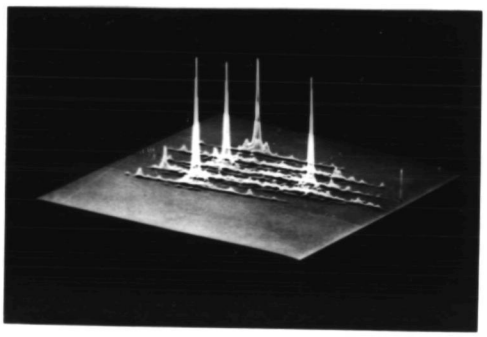

(c) output correlation

Optical pattern recognition performed on the system of Fig. 5.2 [18].

Fig. 5.3

When f was placed at P_1, the output correlation plane pattern in the vicinity of $(x_3, y_3) = (x_0, 0)$ in P_3 appeared as shown in Fig. 3c on an isometric display. Four correlation peaks are observed and their locations are seen to correspond to the four occurrences of the reference word in the full input image [18].

It must be noted that an HOE lens synthesized with an MSF differs from the usual HOE lens described in Sect. 5.1. In our present case, the reference beam used is $H(x_2/\lambda f_L)$, i.e. the Fourier transform of the reference object h(x). It is therefore not uniform and consequently, the diffraction efficiency of the HOE lens will vary across its aperture. This is quite different from the spatially uniform diffraction efficiency of a conventional HOE. We discuss this issue further in Sect. 5.2.3.

5.2.3 ANALYSIS

A feature of this and any MSF optical pattern recognition system is proper selection of the beam balance ratio $K = |u_r/u_s|^2$ used during MSF synthesis [10]. Since u_s varies spatially, so does K. Since the modulation of the MSF is a maximum when K = 1, we can select the spatial frequency band in which to set K = 1 and hence enhance certain spatial frequencies in the input data during MSF synthesis. We refer to this as weighted MSF synthesis [10]. For the input text data of Fig. 5.3a, the stroke width of the input characters was measured to be 0.08 mm. This corresponds to a maximum input spatial frequency of 12.5 cy/mm and a maximum MSF aperture of $2x_b = 2\lambda f_L/0.08 = 7.88$ mm. For the case of this input text data, the FT of the word "PROFESSOR" was found to exhibit peaks at spatial frequencies corresponding to the reciprocal of the: stroke width, spacing between letters, the width of a letter and half the height of a letter.

The FT information in the word is present as modulation about these spatial frequencies [15]. The latter two spatial frequencies (letter width and half-letter height) coincide at 3.7 cy/mm, where a bright FT plane spot is observed. Thus, we adjust K to be one at this spatial frequency during synthesis of the MSF and thus maximize the correlator's performance. This acts as a band-pass filter, which is adequate since the dominant spatial frequencies in the MSF are centered as modulation about the 3.7 cy/mm carrier. Moreso, the HOE recorded at P_2 need only optimally operate over this band of spatial frequencies. Its performance is thus less demanding than that of the normal FT lens. The effect of HOE aberrations appears to be greatly reduced by such weighted MSFs synthesis techniques. The nearly equal intensity of all output correlation peaks in Figure 5.3c indicates the excellent performance of the system and this technique.

In the design of this system and experiment, particular attention was also given to astigmatic aberrations since these are a major error source in such a system [9,16]. We include only third-order aberrations, denote the field angle of the key object by $\tan\beta = \varepsilon/f_1$ and assume $\tan\beta \ll 2x_0/R_o$, where R_0 is the distance from the center of P_2 to $x_3 = x_0$. We then find the optical path difference for the system to be $\Delta r_a \simeq x_2^2 x_0(\tan\beta)/R_0^2$. For an input aperture D, we find $(\tan\beta)_{max} = D/2f_L$. If the maximum input spatial frequency is f_m, then the maximum optical path difference error is

$$\Delta r_{a\ max} = f_m^2 \lambda^2 D f_L \sin\theta/2R_0, \tag{6}$$

where $\sin\theta = x_0/R_0$. In the design of our experimental system, we restricted f_m and D, minimized θ and f_L, while increasing R_0 to maintain large output correlation peak intensities.

As seen in Fig. 5.3c all four of the correlation peaks corresponding to each location of h within f are of nearly the same peak intensity I_p and have

approximately the same SNR. To determine the amount of I_p loss to be expected for a given translation of the input, we used the astigmatic wave aberration equations of Champagne [16] and found the phase aberration due to astigmatism for the system of Fig. 5.2 to be

$$\phi_a = K x_h^2 x_0 \Delta x_3 / R_0^3 \tag{7}$$

where x_h is the aperture of the HOE. The shift Δx_3 in the location of the correlation peak is related to the corresponding shift Δx_1 of h in the input by $\Delta x_3 = R_0 \Delta x_1 / f_L = 0.8 \Delta x_1$ for our experimental system. The maximum MSF aperture is $2x_b = 7.88$ mm from before. Using these values in the quadratic phase model $\phi_a = B x_n^2$, where $x_n = x_h / x_b$, we find $B = 1.6\pi x_b^2 x_0 \Delta x / \lambda R_o^3$. Following [17], we estimate the correlation peak intensity as a function of the lens phase error ϕ_a by $p = 1 - \sigma_\phi^2 = 1 - 4B^2/45$, where σ_ϕ is the standard deviation of ϕ_a over the full aperture. A theoretical plot of p versus Δx_1 is shown in Figure 5.4 for the experimental system used. From this plot, we see that input displacements of ± 10 mm should result in a theoretical loss in output I_p of only 20%. Experimental verification of this equation (Fig. 5.4) showed only 10% loss in I_p. Since the above phase error model assumes the aberrations to exist over the entire 25 cy/mm HOE aperture, whereas the weighted MSF band-passed only the region above 3.7 cy/mm, our experimental performance is expected to be superior to that predicted by theory. Moreso, we see from this initial theoretical analysis and shift-invariant experiment that the aberration effects of a lensless MSF are less than those of a conventional HOE, due to the non-uniform diffraction efficiency and the weighted MSF synthesis step [18].

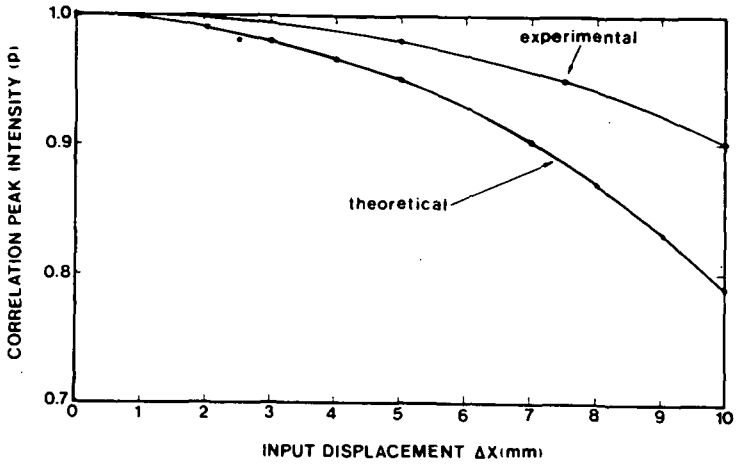

Theoretical and experimental graph of correlation peak intensity versus input displacement for the experiment in Fig. 5.3 on the system in Fig. 5.2 [18].

Fig. 5.4

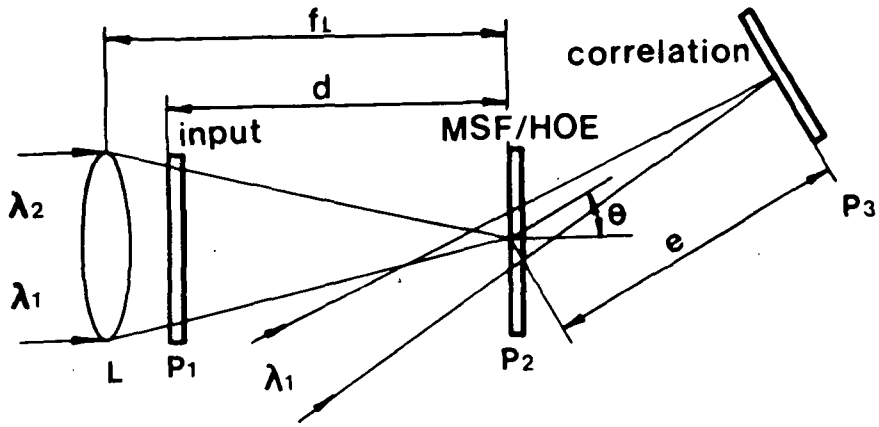

Schematic diagram of a scaling correlator using a lensless MSF.

Fig. 5.5

5.3 WAVELENGTH SCALING CORRELATOR

5.3.1 THEORY

We next consider the off-line synthesis of the lensless MSF at one wavelength (λ_1) and its subsequent use in a correlator illuminated with a second wavelength (λ_2) of light. Such a case arises when a laser diode is used as the light source during correlation. Since MSF materials of adequate holographic quality are not available with good response in the normal wavelength ranges of laser diodes, off-line filter synthesis with a gas laser is necessary. Correlation using a laser diode source then follows.

To account for the $\mu = \lambda_2/\lambda_1$ wavelength change, a scaling correlator [19] (Fig. 5.5 is used. The lensless MSF is formed at P_2 as before, except the input h at P_1 is now placed behind lens L_1. Thus the size of the transform is scaled by f_L/d and an added quadratic phase factor is present. The transmittance of the term of interest in P_2 after development is the conjugate of the term incident on P_2 during filter synthesis. During correlation, the light distribution incident on P_2 contains the original quadratic phase factor. As this light passes through P_2, the quadratic phas factor cancels and we are left with the desired terms leaving P_2. If the distance d between P_1 and P_2 is varied, the scale of the FT can be changed. To satisfy the focusing condition in the full correlator, the scale difference should be kept below 20% in practice [10]. The scaling correlator architecture is necessary in the present system to compensate for the different wavelengths used during recording of the MSF and in correlation. In this system and its many variations [20], the aperture and spatial frequency requirements of HOE-1 are greatly reduced, thus decreasing the effects of lens aberrations in HOE-1.

5.3.2 SYSTEM DESIGN

To model the case of MSF synthesis at λ_1 and correlation at λ_2, an HOE/MSF was formed at P_2 by using normal plane wave illumination (λ_1) of a glass lens L_1. The reference function h was placed at P_1 (a distance d_1 from P_2) and the interference pattern of H (the FT of h) and a converging reference beam was formed at P_2 in λ_1 = 488 nm light. This constitutes synthesis of the combined HOE/MSF at P_2 as described in Sect. 5.2.

During correlation, Fig. 5.5 is still used with the converging reference beam blocked and with L_1 illuminated with λ_2 = 633 nm. To satisfy proper scaling of the FT of the input, the distance d_2 during the correlation was adjusted to satisfy $d_2 = \lambda_1 d_1/\lambda_2$ where $\mu = \lambda_2/\lambda_1 \simeq 1.3$. From [19], we find that we must satisfy $e_2 = e_1/\mu$, where e_1 and e_2 denote the spacing e used during MSF synthesis and correlation respectively. A slight tilt in the orientation of the correlation plane P_3 is also necessary to satisfy $\sin\theta_1 = \mu\sin\theta_2$, where θ_1 is the reference to signal beam angle used during MSF synthesis and θ_2 is the angle necessary during correlation. The displacement Δx_3 of the output correlation peak for a displacement Δx_1 of the input is to first order $\Delta x_3 = (e_2/d_2)\Delta x_1 = (e_1/d_1)\Delta x_1$. If $\Delta x_1 << d_2$ and $x_3 << e_2$, we expect small field angles and distortions and hence an accurate output correlation plane pattern with minimal HOE aberration effects.

5.3.3 EXPERIMENT

For the experiments performed, we chose: $e_1 = d_1 = 400$ mm, $\theta_1 = 17°$, $\lambda_1 = 488$ nm (argon laser), and $\lambda_2 = 633$ nm (He-Ne laser) or $\mu = 1.3$. We adjusted d_2, e_2 and θ_2 as described above. The input image used is shown in Fig. 5.6a.

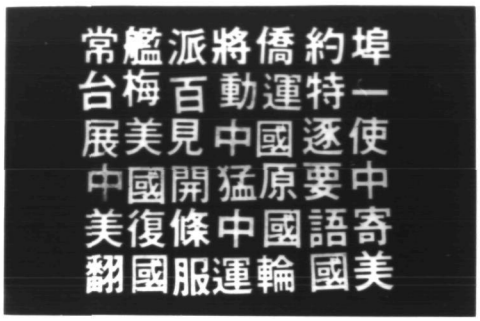

(a) input

(b) reference

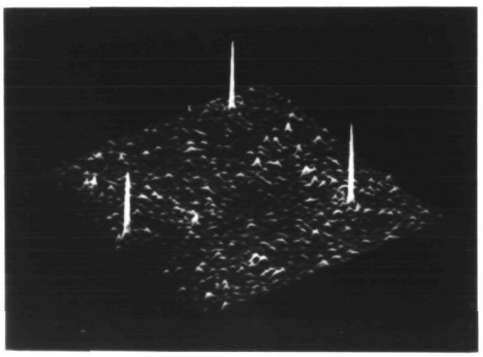

(c) output correlation

Experimental image pattern recognition data obtained using the system in Fig. 5.5 [21].

Fig. 5.6

A combined HOE/MSF of the Chinese word "China" (Fig.6b) was recorded in λ_1 = 488 nm light and placed at P_2. A glass lens was used for L_1 during MSF synthesis to ensure a high quality filter. When the input image of Figure 6a was placed at P_1 and the HOE/MSF at P_2, the three expected output correlation peaks appear [21] as shown in Fig. 5.6c. All output correlation peaks were of comparable SNR and the shift-invariance of the system (with less than 10% change in SNR for ± 10 mm input displacements) was experimentally verified.

5.3.4 DISCUSSION

During synthesis of the MSF at P_2, the beam balance ratio K (the ratio of the intensities of the signal and reference beams) was adjusted to be one in the 3-4 cy/mm spatial frequency range. This weighted MSF technique [10] was again employed to optimize performance of the correlator. This band-pass filtering action appears to reduce the aberration effects of the HOEs as noted in Sect. 5.2.

Formation of HOEs at one wavelength and use of them at another has been studied previously and several design techniques for such lenses have been presented [22-24]. Thus, this issue does not seem to be of major concern, as our experimental demonstrations verified. Many alternate optical system architectures are possible using HOEs. As shown in [25], the point reference source used in formation of an HOE can be placed in any plane; as noted in [26], the recording and reconstructing wavelengths for an HOE can differ, and as discussed in [27], the analysis of an FT formed with spherical wave illumination parallels holographic imaging formuli.

From these data, we conclude that use of an HOE/lensless MSF system in which the HOE and MSF are recorded at λ_1 and the correlation performed at λ_2 is feasible in the scaling correlator system described. Furthermore, with proper attention to system design parameters, a compact laser diode/HOE/lensless MSF correlator system for pattern recognition applications appears promising.

The correlation experiment described in Sect. 5.3.3 and several others were repeated when L_1 in Fig. 5.5 was an HOE. Lower correlation output SNR values resulted. This was attributed to the low diffraction efficiency ($\simeq$3%) of the HOEs and the resultant low detectable correlation output light levels. Use of dichromated gelatin or similar bleached HOEs [2,3] with larger diffraction efficiencies (80%) should improve this light loss. In general, the quality of the HOEs fabricated appears adequate for coherent optical pattern recognition as noted earlier.

5.4 LASER DIODE CORRELATOR

5.4.1 ABERRATION ANALYSIS

As noted at the outset, our major motivation for this study was the use of a lensless HOE/MSF (synthesized off-line with a gas laser) in a correlator using a laser diode source. We now consider such a laser diode/lensless MSF system with attention to proper selection of the system design parameters to minimize aberration effects. We consider the system of Fig. 5.7 with: λ_1 = 633 nm (He-Ne laser), λ_2 = 794.5 nm (ML-4001 laser diode), $e_1 = d_1$ = 400 mm, f_{L1} = 760 mm, a maximum input spatial frequency f_m = 10 cy/mm, a maximum MSF

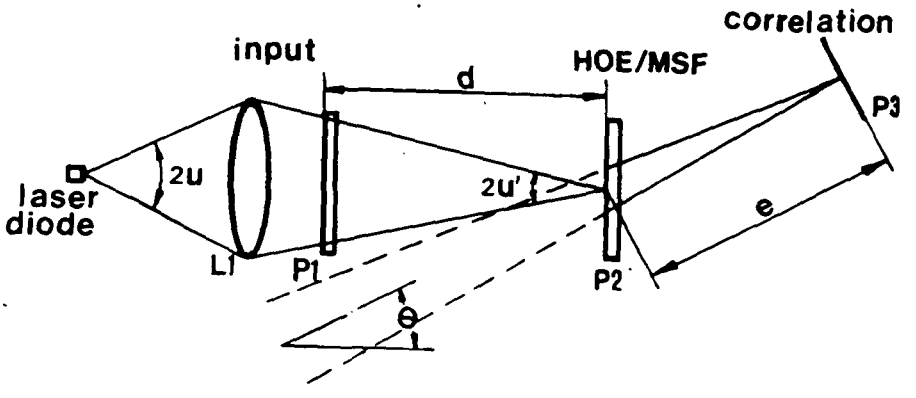

Schematic diagram of a laser diode/lensless MSF correlator [7].

Fig. 5.7

aperture x_m = 2.5 mm, an input aperture of half width Δx_1 = 12.5 mm, and a displacement x_0 = 100 mm of the center of P_3 from the optical axis. With these system parameters, the astigmatic aberration equation of Champagne [16] (with our notation) becomes

$$W_a = (x_m^2/2\lambda_2)[(\mu^3-\mu)x_0^2/e_1^3 + 2\mu^3 x_0 \Delta x_1/e_1^2 d_1 + (\mu^3 \Delta x_1^2/d_1^2)(1/e_1 - 1/d_1)]. \quad (8)$$

For the system parameters indicated, the maximum astigmatism and its rms value were found to be: $W_{a\ max} = 0.44\ \lambda_2$ and $W_{a\ rms} = 0.13\ \lambda_2$. These values are quite adequate to permit high performance from the correlator system. Note that weighted MSF synthesis will reduce these W_a effects even more (as shown in Sect. 5.2). Selecting the system parameters to reduce W_a is quite direct. If the input parameters (f_m and Δx_1) are given, W_a is reduced by decreasing x_0 (which is always much larger than Δx_1). However, if x_0 is less than a certain minimum, overlap of the correlation and other terms leaving the HOE/MSF will occur. Increasing e also controls W_a at the cost of an increased system length. Smaller μ values also reduce W_a, but small wavelength changes are not always possible.

5.4.2 TEMPORAL AND SPATIAL COHERENCE EFFECTS

The temporal coherence of a laser diode is another source of concern. It varies with power and temperature, producing a spectral source width $\Delta\lambda_2$ that will limit [4-6] the useable linear 1-D input space-bandwidth N. One can easily [4-6] express N in terms of laser diode parameters. We first recall that the spatial location x_f of the FT spot corresponding to spatial frequency f_x is related to the wavelength λ_2 of the light used and the focal length f_L

of the FT lens by

$$x_f = f_x f_L \lambda_2. \tag{9}$$

If the wavelength of the source shifts by $\Delta\lambda_2$, the FT spot shift is

$$\Delta x_f = f_x f_L \Delta\lambda_2. \tag{10}$$

The maximum allowable Δx_f due to $\Delta\lambda_2$ should be less than the half width Δx_0 of the zero-order spot (due only to diffraction from input aperture D), i.e.

$$\Delta x_0 = f_L \lambda_2 / D. \tag{11}$$

Requiring $\Delta x_f \leq \Delta x_0$, we find

$$f_x f_L \Delta\lambda_2 \leq f_L \lambda_2 / D, \tag{12}$$

or

$$f_x D \leq \lambda_2 / \Delta\lambda_2. \tag{13}$$

Since $f_x D = N$, the linear 1-D input space bandwidth product, we find that a wavelength shift $\Delta\lambda_2$ of the source λ_2 restricts the useable N to [4-6]

$$N \leq \lambda_2 / \Delta\lambda_2, \tag{14}$$

or the reciprocal of the fractional wavelength change.

For the ML-4001 single-mode Mitsubishi laser diode used, $\Delta\lambda_2 = 0.2$ nm is specified. Temperature effects can be expected to shift the source's wave-

length by a maximum of $\Delta\lambda_2$ = 2 nm, in which case N should be restricted to 400 points per line. This is less than 512 line television resolution, but the above analysis is worse-case, since considerable spatial frequency data below the maximum is usually the major contribution to the correlation. We thus expect the system to operate on television resolution input data.

The source's spectral width $\Delta\lambda_2$ also produces a divergence $\Delta\theta_2$ in the wavefront leaving P_2 during correlation and hence affects the shape of the correlation peak. To reduce the effects of $\Delta\lambda_2$ on the drop of the correlation peak, we require $e_2\Delta\theta_2$ (the spot broading) to be less than half the diffraction limited correlation peak width.

An analysis of this effect follows. The carrier spatial frequency recorded on the MSF/HOE is

$$\alpha = \sin\theta_1/\lambda_1 = \sin\theta_2/\lambda_2. \tag{15}$$

After differentiation, we find

$$\Delta\theta_2 = \Delta\lambda_2\sin\theta_1/\lambda_1\cos\theta_2, \tag{16}$$

From which,

$$e_2\Delta\theta_2 = \mu e_2\Delta\lambda_2\sin\theta_1/\lambda_2\cos\theta_2 \tag{17}$$

The half peak width due to diffraction is

$$e_2\lambda_2/(2x_m\cos\theta_2),$$

where $2x_m\cos\theta_2$ is the entire diffraction aperture of the MSF/HOE. Requiring

$e_2\Delta\theta_2 \leq e_2\lambda_2/(2x_m\cos\theta_2)$ yields the condition

$$\Delta\lambda_2 \leq \lambda_2^2/(2\mu x_m \sin\theta_1) \ . \qquad (18)$$

For our system, x_m = 2.5 mm, sin θ_1 = 0.25, μ = 1.26, λ_2 = 795.4 nm and the spectral width of the source should thus be less than 0.4 nm. A change in device temperature will result in a wavelength shift rather than an increase in the spectral width of the source. Only the $\Delta\lambda_2$ spread (rather than the λ_2 shift) affects the shape of the correlation peak. Since the specified $\Delta\lambda_2$ = 0.2 nm for the laser diode used is less than the above requirement of 0.4 nm, no problem is foreseen in this regard with our indicated design. To reduce $\Delta\lambda_2$ effects, small θ (i.e. small x_0) and small μ values are again desirable as in Sect. 5.4.1.

The spatial coherence of the laser diode source used was also considered. This parameter was obtained from measurements of the fringe visibility of the P_2 pattern formed by interference of two 5 mm diameter apertures separated horizontally and then vertically in P_1 by 25 mm. Contrast ratios of 0.77 and 0.75 were measured for the horizontal and vertical interference patterns respectively. From [28], we define the fringe visibility as the ratio of coherent intensity I_c to total intensity I_t. The laser diode used thus gave V = 0.77 and 0.75 horizontal and vertical respectively. To determine the effects of V on performance of the correlator, we assume uniform illumination at P_1 (see Sect 5.4.3). Since the correlator's output is due to the coherent light contribution, we expect the correlation peak intensity I_p to be proportional to I_c. We thus expect I_p and SNR of the output correlation to be decreased by a factor V due to the limited (V $\neq$ 1) spatial coherence

of the laser diode used. Thus, as the location of the input object shifts from the center to the edge of P_1, we anticipate a loss of V or 1.2 dB in correlation SNR.

5.4.3 LASER DIODE COLLIMATION

Another concern in the use of a laser diode is proper source collimation. If the entire aperture angle of the laser diode is $2u = 10°$ (see Fig. 7) and the wavelength of the laser diode is 0.795 μm, then the main lobe due to aperture diffraction will have a width of 4.6 μm. Therefore, the small (1-2 μm) emission area of the laser diode used allows us to consider it as a point source, that is more or less equivalent to the diffraction limit of the optical system. The above example also indicates that the aperture angle from the laser diode should be restricted to some degree.

In the laser diode scaling-correlation system in Fig. 5.7, a suitable convergent coherent beam incident on P_1 is needed whether the beam is parallel or not before the first Fourier transform lens. The convergence angle of the laser diode and the above diffraction limited resolution analysis enable us to use the simple imaging optical system shown for L_1 in Fig. 5.7. Lens L_1 then requires quite modest specifications. It could be a simple cemented doublet, which can be corrected for spherical aberration. We thus obtain the greatly simplified and compact correlator shown that uses one glass imaging lens and a HOE/MSF element.

Since the radiant intensity distribution of a laser diode is different in orthogonal directions, some added attention is needed to lens system L_1. As the distance from L_1 to the source is increased (i.e. the aperture angle u is decreased), the illumination of P_1 will become more uniform but less light power

will enter the input aperture. We must thus make a choice between the uniformity of illumination and the power that can be used in selecting the distance from source to L_1 and the aperture angle u.

For the ML-4001 laser diode, its full irradiance angle at half power was 10° (vertical) and 40° (horizontal). We assume a Gaussian intensity distribution for the light. Then the light intensity I_u at the aperture is

$$I_u = I_o \cdot e^{-\frac{1}{2} u^2/\sigma^2} , \tag{19}$$

where I_o is the intensity at the center of the aperture and σ is the standard deviation. In the more critical direction (vertical), $I_u = 0.5\ I_o$ when $u = 5^o$ and then $\sigma = 4.25^o$. We chose the spacing from L_1 to the source to intercept a 7^o cone angle subtended by the input aperture. For this system, $u = 3.5^o$ and only one-sixth of the light from the source is used. Using (19) we find $I_u = 0.7I_o$ at the edges of the P_1 aperture. This indicates that the ratio of the correlation peak intensity at the center and edge of the plane will be 0.7 or only about 1.5 dB.

Both $V \neq 1$ and $I_u \neq I_o$ will affect the system's shift-invariance, i.e. the variation in I_p and SNR with location of the correlation peak. For the system design chosen, the effects of spatial coherence and uniformity of illumination are nearly equal (each results in a 1.2 - 1.5 dB maximum I_p and SNR loss).

5.4.4 EXPERIMENT [7]

All the above analysis issues were incorporated into the design of an experimental system in the topology of Fig. 5.7. In Fig. 5.8 we show the input, reference and output correlation plane pattern obtained with the MSF formed at λ_1 = 488 nm and correlation performed with a laser diode at λ_2 = 795.4 nm. The input transparency used was a radar image with a 24 mm x 30 mm format. The SNR of the correlation is quite good as shown even though the reference was located at the edge of input scene.

5.5 SUMMARY AND CONCLUSIONS

A small size and weight optical correlator suitable for airborne applications has been described, designed, analyzed, fabricated, tested and successfully demonstrated. The system employs holographic optical elements in a lensless MSF architecture with improved system alignment and stability features. The light source used during correlation was a laser diode. It was thus necessary to record the matched spatial filter at one wavelength and perform the correlation at the different wavelength of the laser diode. A scaling correlator architecture was used to accomodate the wavelength change and a simple imaging input lens is needed to focus the laser diode onto the filter. A complete system design and analysis including aberration effects and with attention to the system's shift-invariance was performed. The experimental results obtained verified the usefulness of this system.

(a) input

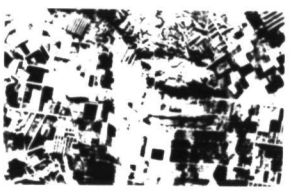

(b) reference

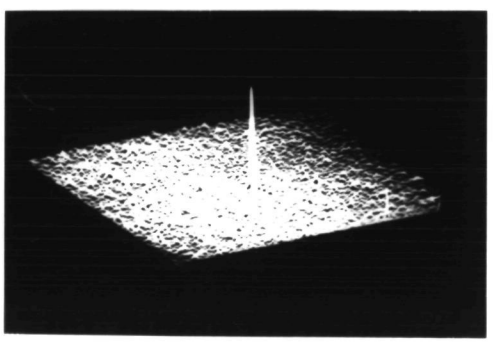

(c) output correlation

Experimental image pattern recognition data obtained using the system in Fig. 5.7 [7].

Fig. 5.8

6. SUMMARY

6.1 SUMMARY

The results of this brief effort were all very encouraging. Our OPR experiments indicated that an optical correlator could easily maintain large and acceptable output correlation plane recognition of LANDSAT data even in the case when various image differences were present in the data. A component assessment of an airborne optical correlator showed that such a system could be fabricated with existing components. A new laser diode/holographic optical element optical correlator using a lensless matched spatial filter with decreased component positioning tolerances was designed, fabricated, demonstrated and analyzed.

6.2 HIGHLIGHTS

The highlights of our eight-month program are:

(1) An image-difference data base of LANDSAT imagery has been assembled.

(2) OPR techniques proved adequate for correlation of LANDSAT data for every image difference considered.

(3) An initial image content and image classification description has been established.

(4) Many aspects of correlations with image differences present have been clarified and demonstrated.

(5) The components for an airborne optical pattern recognition system appear to exist at present.

(6) A new low-size, low-cost and low-weight optical correlator system for possible airborne use was developed and demonstrated.

REFERENCES

1. A. Van der Lugt, IEEE, IT-10, 139 (1964).
2. B. Chang and C. Leonard, Applied Optics, 18, 2407 (1979).
3. B. Chang, Soc. Photo. Instru. Engrs., 177, 71 (1979).
4. B. Guenther, et al., IEEE, QE-15, 1348 (1979).
5. J. Duthie, et al., Soc. Photo Instru. Engrs., 231 (April 1980).
6. C. Calderone, Final Report on Contract DAAK 40-77-C-0089 (17 December 1979) Grumman Aerospace Corporation.
7. F. Caimi et al., Appl. Opt., 19, 2653 (August 1980).
8. W. Maloney, Applied Optics, 10, 2127 (1971).
9. M. Bage and M. Beddoes, Applied Optics, 15, 2830 (1976).
10. D. Casasent and A. Furman, Applied Optics, 17. 1652, 1662 (1977).
11. G. Groh, Applied Optics, 7, 1643 (1968).
12. D. Gabor, Optica Acta., 16, 519 (1969).
13. S. Ragnarsson, Phys. Ser., 2, 145 (1970).
14. R. Binns, Applied Optics, 7, 1047 (1968).
15. D. Casasent, et al., Optical Engr., July 1980.
16. E. Champagne, J. Opt. Soc. Amer., 57, 51 (1967)
17. T. Luu and D. Casasent, Applied Optics, 18, 791 (1979).
18. M. Shen, et al., Optics Communic., 34, 311 (September 1980).
19. A. Van der Lugt, Applied Optics, 5, 1760 (1966).
20. B. Pernick, Applied Optics, 19, 651 (1980).
21. M. Shen, et al., Optics Communic., 34, 316 (September 1980).
22. S. Bennett, Applied Optics, 15, 542 (1976).
23. M. Latta and R. Pole, Applied Optics, 18, 2418 (1979).

24. N. Lessing, Applied Optics, 19, 487 (1980).

25. J. Castaneda and S. Sandoval, Applied Optics, 18, 3550 (1979).

26. J. Castaneda, J. Altaminano and S. Sandoval, Applied Optics, 19, 485 (1980).

27. J. Ojeda-Castaneda, Appl. Opt., 19, 1386 (1980).

28. M. Born and E. Wolf, Principles of Optics (3rd edition, 1956) p. 503-506.

1. Report No.	2. Government Accession No.	3. Recipient's Catalog No.
NASA CR-165757		

4. Title and Subtitle	5. Report Date
OPTICAL PROCESSING FOR LANDMARK IDENTIFICATION	1 September 1981
	6. Performing Organization Code

7. Author(s)	8. Performing Organization Report No.
David Casasent and Thanh Ky Luu	
	10. Work Unit No.

9. Performing Organization Name and Address	11. Contract or Grant No.
Carnegie-Mellon University Department of Electrical Engineering Pittsburgh, Pennsylvania 15213	NAS1-16125
	13. Type of Report and Period Covered
12. Sponsoring Agency Name and Address National Aeronautics and Space Administration Washington, D.C. 20546	Contractor report
	14. Sponsoring Agency Code

15. Supplementary Notes

Langley technical monitor: Gale Wilson
Final Report

16. Abstract

A study of optical pattern recognition techniques, available components and new airborne optical systems for use in landmark identification was conducted and achieved promising results. A data base of imagery exhibiting multi-sensor, seasonal, snow and fog cover, exposure, and other differences was assembled. These were successfully processed in a scaling optical correlator using weighted matched spatial filter synthesis.

Distinctive data classes were defined and a description of the data (with considerable input information and content information) emerged from this study. It has considerable merit with regard to the preprocessing needed and the image difference categories advanced. A new optical pattern recognition system suitable for airborne applications was developed, assembled and demonstrated. It employed a laser diode light source and holographic optical elements in a new lensless matched spatial filter architecture with greatly reduced size and weight, as well as component positioning toleranced.

17. Key Words (Suggested by Author(s))	18. Distribution Statement
Correlation, Holographic Optical Elements, Laser diode, Lensless matched filter, Matched spatial filter, Optical processor, Pattern recognition	Unclassified-Unlimited

19. Security Classif. (of this report)	20. Security Classif. (of this page)	21. No. of Pages	22. Price
Unclassified	Unclassified	67	

For sale by the National Technical Information Service, Springfield, Virginia 22161